Understanding Low-Energy Nuclear Recoils in Liquid Xenon for Dark Matter Searches and the First Results of XENON1T.

Matthew Duschl Anthony

Submitted in partial fulfillment of the
requirements for the degree of
Doctor of Philosophy
in the Graduate School of Arts and Sciences

COLUMBIA UNIVERSITY

2017

ABSTRACT

[Title]

[Author]

[Abstract Text]

Contents

List of Figures

Acknowledgements

[Acknowledgments]

[Dedication]

Chapter 1

Dark Matter

For nearly a century, experimental evidence has suggested that a large portion of the universe is made up of a non-luminous type of matter. While this dark matter has only been detected indirectly via its interaction with normal matter through the gravitational force, recent experiments conclude that approximately 26% of the entire energy density of the universe is comprised by dark matter.

In this chapter, I will focus on the leading dark matter model, the experimental evidence for its existence, the different candidates for particle dark matter, and the current detection methods employed in the search for particle dark matter.

1.1 ΛCDM Model

One of the guiding principles of cosmology are the assumptions that the universe is both homogeneous and isotropic at large enough scales (typically on the order 100 Mpc or 10^5 light years). Continuing with these principles and maintaining generality, we can arrive at the Robertson-Walker space-time metric

$$ds = -c^2dt^2 + a(t)^2\left(\frac{dr^2}{1-kr^2} + r^2d\Omega^2\right) \tag{1.1}$$

Here, $a(t)$ is called the *scale factor*, an arbitrary function of time allowing for time dependent changes of the universe, and k is a constant modeling the curvature of the universe. For $k = -1$, the universe is considered open, for $k = 1$, the universe is considered closed, and at $k = 0$ we are left with our Euclidean (flat) universe. Note that for $a(t) = 1$ and $k = 0$ the Robertson-Walker metric reduces to the Minkowski metric.

Using this metric in combination with Einstein's equation we can derive the equations for the Friedmann-Robertson-Walker universe described by the Friedmann equations.

$$\frac{\ddot{a}}{a} = -\frac{4\pi G}{3}(\rho + 3p) \tag{1.2}$$

$$\left(\frac{\dot{a}}{a}\right)^2 = \frac{8\pi G}{3}\rho - \frac{k}{a^2} \tag{1.3}$$

We can define several useful (and commonplace) parameters to simplify the second Friedmann equation further.

Hubble Parameter: $H = \frac{\dot{a}}{a}$
Critical Density: $\rho_{crit} = \frac{3H^2}{8\pi G}$
Density Parameters: $\Omega_i = \frac{8\pi G \rho_i}{3H^2} = \frac{\rho_i}{\rho_{crit}}$

$$\Omega - 1 = \frac{k}{H^2 a^2}, \qquad \Omega = \sum_i \Omega_i = \Omega_\Lambda + \Omega_{CDM} + \Omega_{Baryon} + \Omega_{Rad} \dots \tag{1.4}$$

Here the critical density is defined such that the universe is flat ($k = 0$). One can think of $\frac{\Omega_i}{\Omega}$ as what part of the total matter and energy budget a particular component makes up. The main contributors to the density of the universe are dark energy and cold dark matter hence the ΛCDM Model. The density parameters give insight into the large scale structure of the universe and measurements of the various density parameters and other ΛCDM parameters has been a major focus of research over the last two decades and will be discussed later in this chapter [**carroll1997lecture**].

1.2 Evidence of Dark Matter

1.2.1 Dynamical Constraints from Clusters of Galaxies

The first evidence of dark matter came from Fritz Zwicky in 1933. Zwicky used a basic application of the virial theorem on galaxies in the Coma Cluster to estimate the mass of the cluster. He then estimated the total mass based on the brightness of the cluster and found significant disagreement between the results leading him to the conclusion that “if this would be confirmed we would get the surprising result that dark matter is present in much greater amount than luminous matter” [1].

Figure 1.1: A composite image of the Coma Cluster combining X-ray data and optical data. The gas in the cluster is shown in purple. Image Credit: X-ray - NASA/CXC/MPE/J.Sanders et al, Optical - SDSS

1.2.2 Dynamical Constraints from Galactic Rotation Curves

Nearly fourty years later, stronger evidence was provided for the existence of dark matter by Vera Rubin and Kent Ford in their 1970 paper looking at the rotation curve of the Andomeda Galaxy [3]. In this paper, Rubin used the Hα lines to determine the orbital velocities of different stars in the galaxy. Later measurements used the 21 cm hyperfine transition line to measure orbital velocities within other galaxies [2].

From simple Newtonian arguments, one gets the following description of the orbital velocity inside a galaxy:

$$v(r) = \sqrt{\frac{GM(r)}{r}} \tag{1.5}$$

In this equation, M(r) is the sum of all the mass within a radius r. Under the assumption that most of the mass is concentrated at the center of the galaxy (in the form of a supermassive blackhole), one would expect that at large distances from the center of the galaxy, the orbital velocity would fall off as $v \propto r^{-1/2}$.

However, what is seen differs from this simple approximation drastically. Fig. 1.2 is taken from Ref. [2] but the results are similar to what Rubin and Ford saw deecades earlier: the asymptotic behavior of the orbital velocity is constant and does not show any polynomial roll-off. By isolating the contributions from measurable mass densities (such as visible matter and gas), one can get an idea of the density distribution of dark matter in a galaxy. From the figure below, one could asymtotically estimate that $M(r) \propto r$ which would imply that $\rho(r) \propto r^{-2}$. One quickly realizes that this

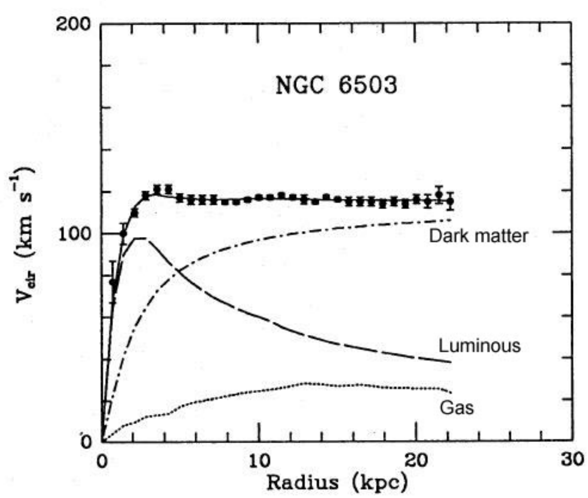

Figure 1.2: The rotation curve of the galaxy NGC 6503 broken down into individual components: visible matter (dashed), gas (dotted), and dark matter (dash dotted) [2].

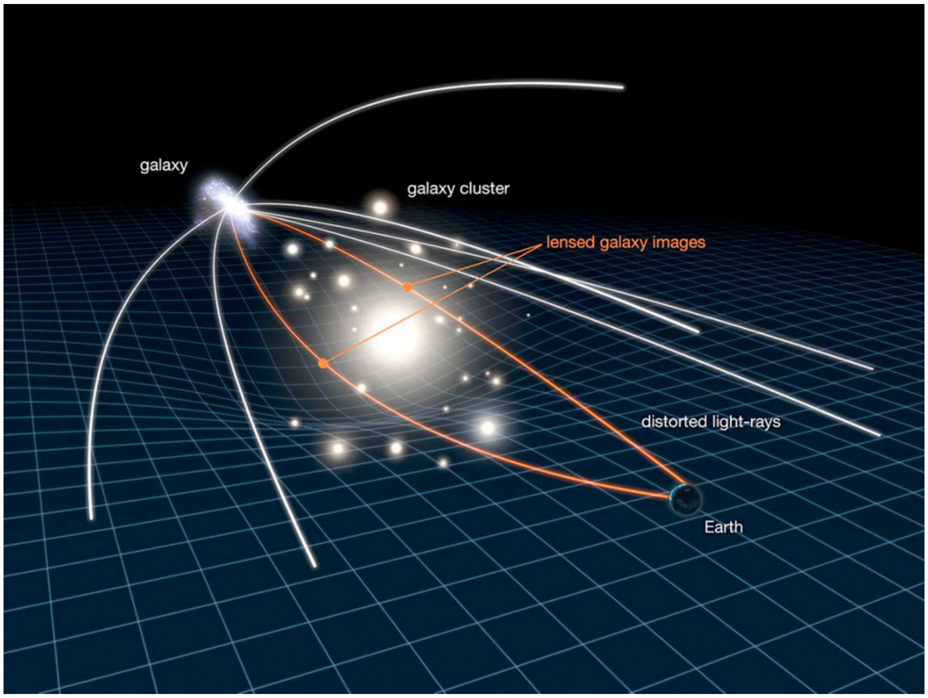

Figure 1.3: A cartoon showing the deflection of light due to the warping of spacetime caused by the presence of a massive galaxy cluster. Note that for very strong lensing, one expects multiple images of the source object and sometimes even an Einstein Ring around the lense. Image Credit: NASA/ESA.

cannot be the true density since the mass of the galaxy diverges but approximates the density within an effective radius.

1.2.3 Evidence from Graviational Lensing

Gravitational lensing is the distortion of light coming from a source due to the warping of spacetime from the presence of large amounts of matter or energy. This effect is illustrated in Fig. 1.3 and actually captured in the form of an Einstein Cross in Fig. 1.4. In a gravitational lensing system, if we know the redshift (distance) of the source and the lense, we can estimate the gravitational field of the lensing system and hence its mass.

Mass estimation via gravitational lensing in itself is very useful for finding large discrepancies in mass from known sources and true mass (the discrepancy being attributed to dark matter). However, when combined with x-ray measurements, as

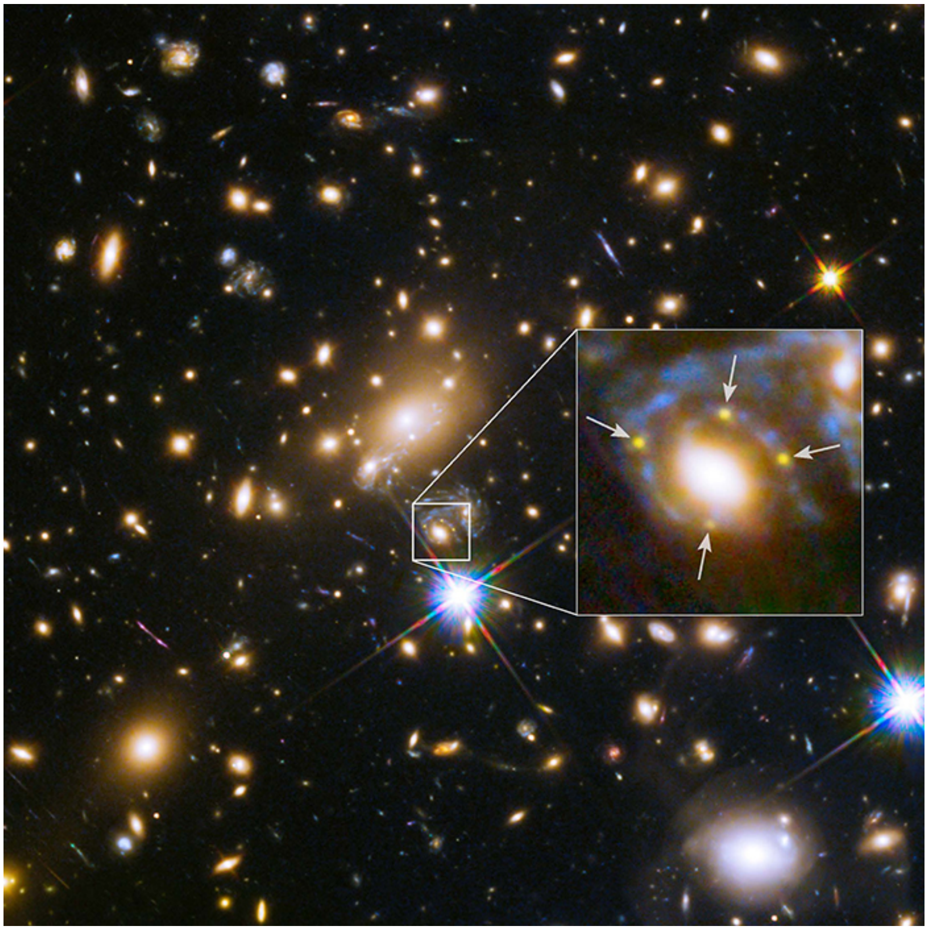

Figure 1.4: In this optical image you see the massive MACS J1149.6+2223 cluster. In the zoomed portion, you can actually see the same supernova, SN Refsdal, in four smaller images around a large galaxy within the cluster. Image Credit: HST.

seen in Fig. 1.5, one gets even more interesting results. Shown in Fig. 1.5 is the Bullet Cluster (1E0657-558) which actually consists of two colliding sub-clusters. In the image on the left, one can see the infrared image from Magellan that is used, along with optical images from Hubble, to estimate the mass distribution of each galaxy cluster through graviational lensing. In the right image, one can see the X-ray map of the Bullet Cluster from the Chandra X-ray observatory with the same mass contours: one can see that the plasma from the clusters interacts giving the cone shapes in the center. However, the mass contours largely remained centered on the individual clusters (as seen in the optical image) implying that the majority of the matter interacted minimally during the collision [4]. Since we know that the galaxies

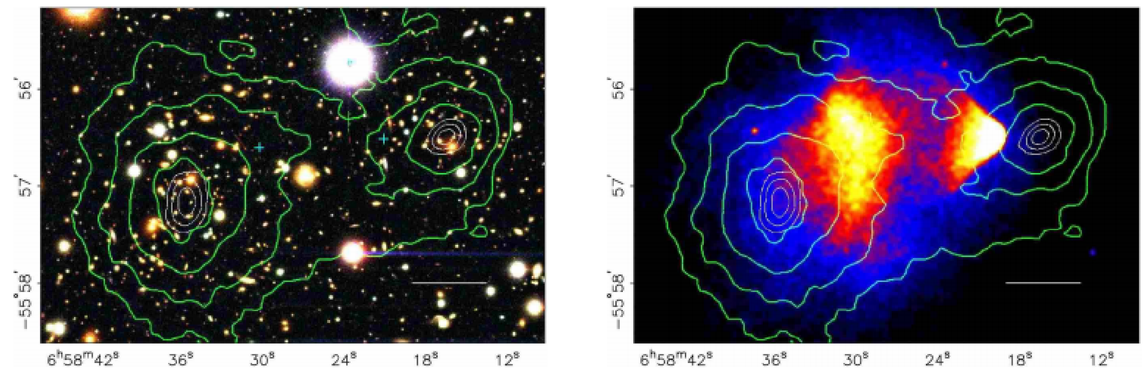

Figure 1.5: Infrared (left) and X-ray (right) maps of the Bullet Cluster (1E0657-558). While the plasma in the clusters interacts during the collision of the two individual clusters, as is seen by the shockwave in the center, the majority of the mass passes right through [4].

make up only a small fraction of the mass in a cluster from the virial theorem, this implies that the dark matter hardly interacts with itself or ordinary matter.

1.2.4 Evidence from the Cosmic Microwave Background

The Cosmic Microwave Background (CMB) has proven to be one of the richest discoveries in all of cosmology. Accidentally discovered in 1964 by Penzias and Wilson [5], the radiation from the CMB is almost perfectly isotropic and described by a blackbody spectrum at 2.725 K [6]. The isotropy in the CMB provides the strongest evidence to date of the Big Bang Hypothesis and helped to formulate our current picture of the early universe down to the recombination epoch, where the universe was sufficiently cool such that hydrogen could form from the free electrons and protons in turn allowing photons to travel freely through the universe.

As the CMB has been studied in more detail, cosmologists began to see that there are in fact very small temperature fluctuations on the order of $\lesssim 100\mu K$ [7–9]. These temperature fluctuations, as seen in the 2015 measurement of the CMB by the Planck satellite, are shown in Fig. 1.6. To characterize the temperature fluctuations of the entire sky, we use the spherical harmonics, $Y_{lm}(\theta, \phi)$.

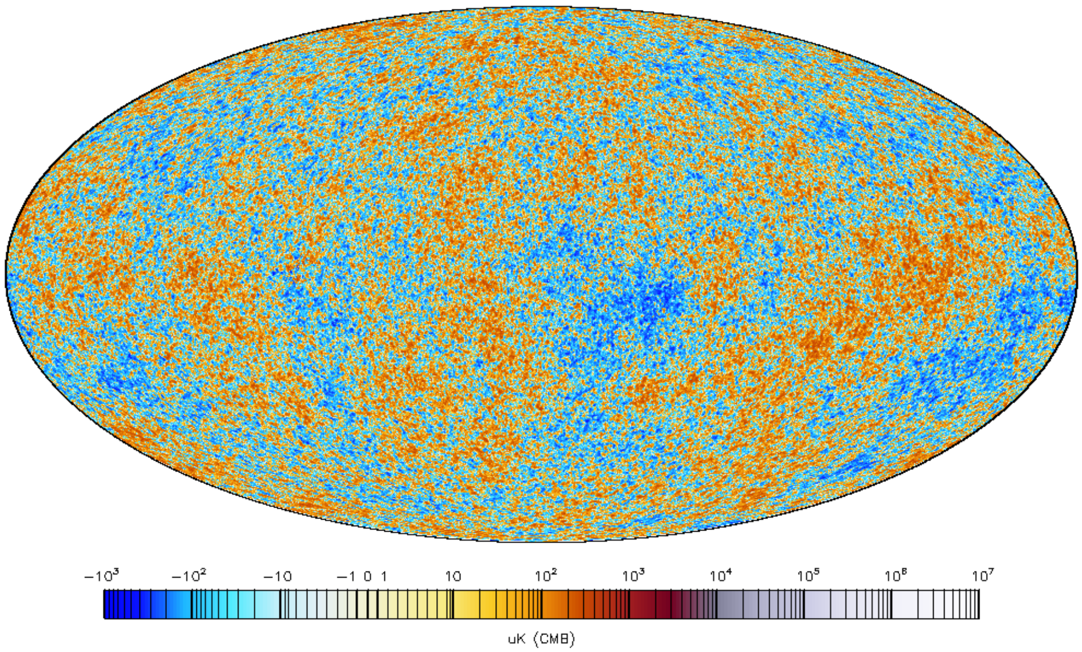

Figure 1.6: The Planck 2015 measurement of the temperature anisotropy of the CMB. Note that the largest deviations from the mean are on the order of $200\mu K$ from the 2.725 K mean (roughly 1 in 10^4). Image Credit: IRSA, Ref. [7].

$$T(\theta, \phi) = \sum_{l=0}^{\infty} \sum_{m=-l}^{l} a_{lm} Y_{lm}(\theta, \phi) \tag{1.6}$$

We assume that the distribution of a_{lm} should be described by a Gaussian distribution, as predicted by inflation, with a mean of 2.725 K for any given multipole moment l. Therefore, the only piece missing to completely describe these a_{lm} for each multiple moment is the variance of this distribution so we define $C_l \equiv \langle |a_{lm}|^2 \rangle$. These C_l form the power spectrum of the CMB and can be used to test various formation models of the universe. Planck tested the ΛCDM model described in Sec. 1.1 against their power spectrum (Fig. 1.7) and found remarkable agreement between prediction and data while constraining some of the universal constants including H_0, Ω_Λ, Ω_{CDM}, Ω_{Baryon}, and Ω_{Rad}. It is from this fit that we find that our universe has a curvature very close to zero and therefore is flat and that our universe is comprised of roughly 68.3% dark energy, 26.8% dark matter, and 4.9% ordinary matter [7].

The ΛCDM model has been tested since its inception using N-body simulations

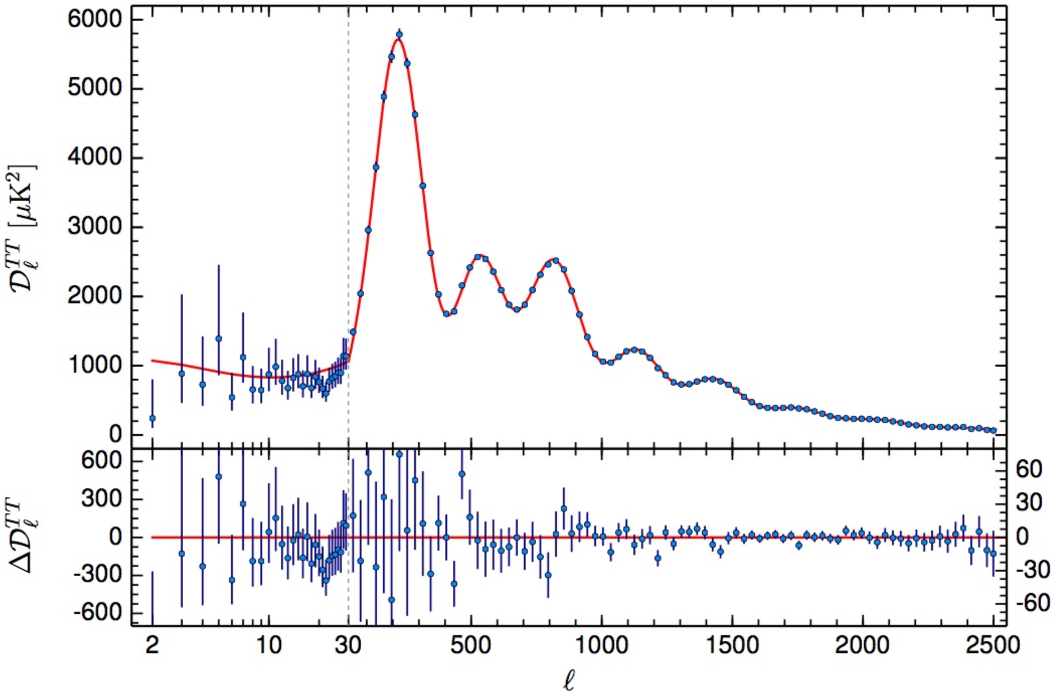

Figure 1.7: The power spectrum of the temperature anisotropies measured by Planck along with the best fit prediction from the ΛCDM model. $\mathcal{D}_l^{TT}$ is a proxy for C_i and is defined $\mathcal{D}_l^{TT} \equiv l(l+1)C_l/2\pi$. Image Credit: Ref. [7].

to propagate the formation of large scale structure in the universe. While small discrepancies between simulation and observation have been found, it is clear from these simulations that without cold dark matter it is extremely difficult to explain the large scale structure we see in the universe given the anisotropies of the CMB [10–12].

1.3 Dark Matter Candidates

While there is an abundance of evidence to suggest that dark matter exists, we have little evidence to suggest what this cold dark matter actually is. In this section, we will discuss two of the most popular candidates for dark matter and their physical motivations. It should be noted that the candidates discussed do not form an exhaustive list but do satisfy the most basic requirements of a dark matter candidate:

- The lifetime of the particle is much greater than the lifetime of the universe (or is stable)
- The particle must be electrically neutral and very weakly interacting with ordinary matter
- The particle must be able to provide the correct relic density of cold dark matter as predicted by the CMB

1.3.1 Axions

Axions are hypothetical standard model particles that are introduced via the Peccei-Quinn mechanism as a solution to the strong-CP problem, one of the largest remaining deficiencies in the standard model [13]. CP (charge and parity) symmetry violation is required to explain the imbalance of matter and antimatter in the universe (why more matter exists) and has been observed in electroweak theory in a wide variety of measurements [14–18]. CP violation has never been observed in quantum chromodynamics even though there are natural terms in the QCD Lagrangian that would allow it. Therefore, this term in the Lagrangian, must be fine-tuned to exactly zero, hence the strong-CP problem. The axion introduced by Peccei-Quinn theory replaces this term with a field and gives the Lagrangian natural CP symmetry.

While the discovery of the axion would solve one of the largest problems of standard model, it also has the potential to solve one of the largest open mysteries of cosmology by making up at least a part of the cold dark matter density of the universe. Even though the axion is expected to have a very small mass ($10^{-6} - 10^{-2}$ eV) it could still be produced cosmologically such that the large scale structure that we observe in the universe today is explained and we arrive at the CDM density estimated by Planck [19].

There are a number of experiments that can provide information about axions, both directly and indirectly. The mass range of axions, is essentially restricted from cosmological evidence from the CMB and stellar evolution. Simultaneously, cavity microwave experiments such as ADMX [20] and NMR based searches such as CASPeR [21] try to directly detect these low mass CDM candidates.

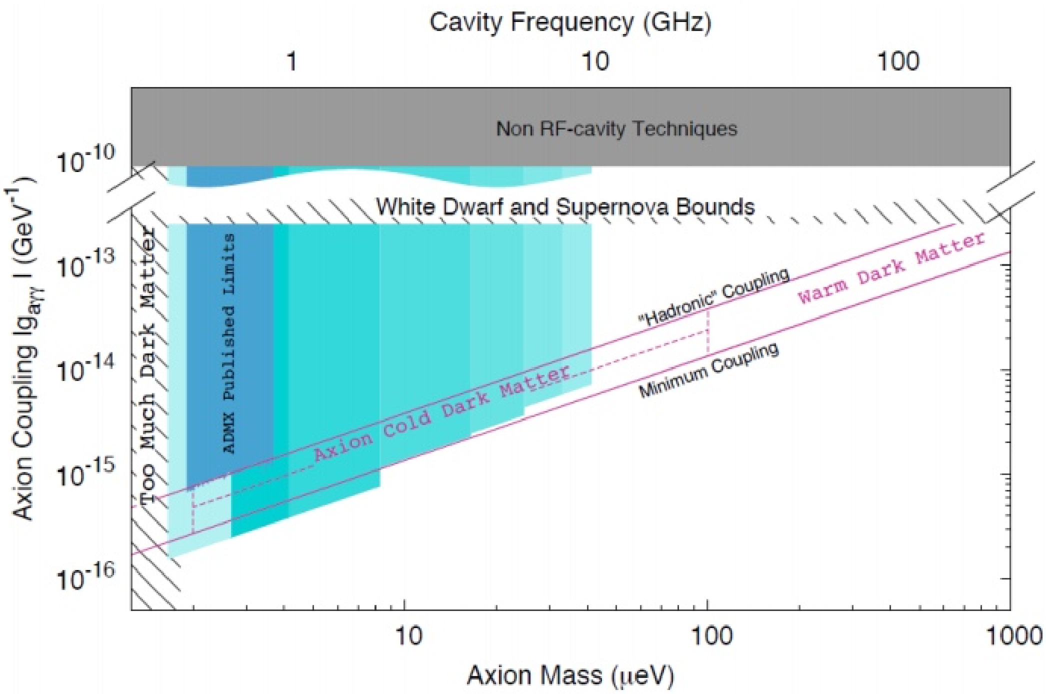

Figure 1.8: The projected sensitivity of the ADMX Generation 2 axion search (shaded regions). Note that strong cosmological constraints are placed on the mass range and the axion coupling is also constrained by the mass. The ADMX collaboration predicts that the searches shown will be completed by 2022 [20].

1.3.2 WIMPs

Weakly interacting massive particles (WIMPs), which will be the focus of the remainder of this work, have proven to be the most popular dark matter candidate historically. WIMPs not only satisfy the basic criteria listed at the beginning of this section but additionally they have what is referred to as the "WIMP Miracle" in their favor. In the early stages of the universe, the temperature and density were so large that all particles were in a state of chemical equilibrium. A dark matter particle could annihilate by colliding with its anti-partner to form any type of particle and vice versa. As time passed, however, the universe expanded and cooled making it more unlikely for these dark matter particles to be created or destroyed. Using this thermal equilibrium model alongside the ΛCDM model, one can infer that the CDM density in the universe today is approximately given by [22, 23]

$$\Omega_{CDM}h^2 \approx \frac{3 \times 10^{-27}\text{cm}^3\text{s}^{-1}}{\langle \sigma_{ann} v \rangle} \tag{1.7}$$

where $\langle \sigma_{ann} v \rangle$ is thermally averaged annihilation cross-section of cold dark matter. Incredibly enough, if we assume that cold dark matter has properties such as cross-section and mass on the weak scale, we find that $\Omega_{CDM}h^2 \approx 0.1$, which is in agreement with cosmological constraints.

In addition to WIMPs agreeing with cosmological evidence, several WIMP-like particles having masses on the order of 100 GeV with very long lifetimes naturally fall out of extensions of the standard model, such as supersymmetry.

1.4 Detecting WIMPs

Over the last few decades there has been an enormous concerted effort to detect WIMPs. This effort has been focused in three general approaches: indirect detection, collider detection, and direct detection. Fig. 1.9 shows the idea behind these approaches:

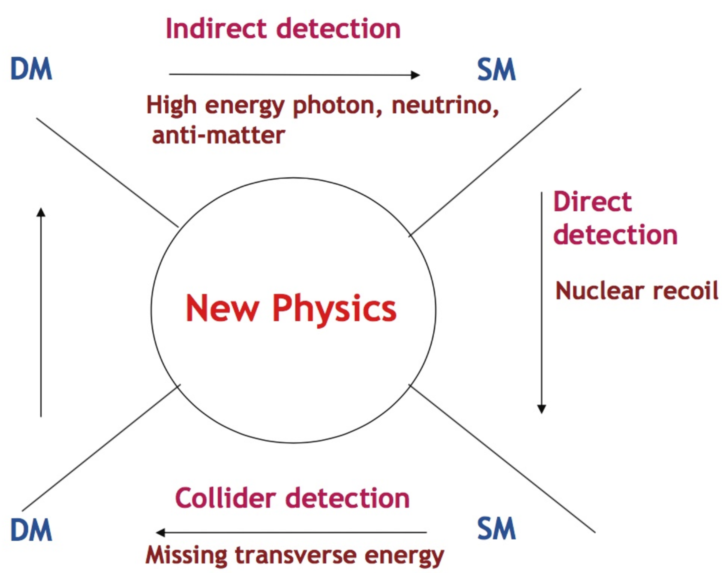

Figure 1.9: The three general approaches to WIMP detection: indirect detection, collider detection, and direct detection. Image Credit: [24].

- Indirect detection looks for the annihilation of WIMPs in our galaxy into ordinary matter
- Collider detection is an attempt at creating WIMPs by colliding ordinary matter
- Direct detection looks for the scattering of WIMPs with ordinary matter

In this section we will discuss these three detection approaches with an emphasis on direct detection. We will conclude with a brief discussion of the current direct detection experiments and notable results from this sector.

1.4.1 Indirect Detection

As we know from previous sections, WIMPs, if they make up all (or some) of the dark matter in the universe, must reside in galaxies to explain the odd behavior of rotation curves and the mass discrepancies. Given the observational evidence, simulations have been created that can predict both the distribution of dark matter within our own and other galaxies [25, 26] and the density of dark matter in our own solar system (roughly $0.2 - 0.4\,\frac{\text{GeV}}{\text{cm}^3}$ [27]). Indirect detection experiments look at high density regions of dark matter halos, such as in or around the Milky Way center and dwarf galaxies, to search for annihilations of WIMPs into detectable particles.

The goal of indirect detection is to capture a dark matter annihilation by observing its byproducts. In the ideal case, two dark matter particles would annihilate and create two photons with energies equal to the mass of the dark matter particle. Even though this would be the "smoking gun" evidence of dark matter, most of the standard model extension WIMPs predict that this would be highly suppressed. Instead, these indirect experiments are more likely to observe the annihilation of WIMPs into other particles which in turn will produce photons [24].

A major difficulty in indirect detection experiments is distinguishing potential signals from normal astrophysical processes. Since areas of high dark matter density are also typically areas of high astrophysical activity it becomes difficult to separate potential dark matter signals from potentially new astrophysics [28]. However, in recent years, astrophysicists have started turning their telescopes towards dwarf galaxies, which are dark matter dominated but have negligible astrophysical backgrounds [29].

1.4.2 Collider Detection

The main idea behind collider detection is that since the WIMP is expected to have a mass on the order of $1 - 10^3$ GeV we can create it in particle accelerators. Of course, detectors at particle accelerators are not designed to detect dark matter directly so when searching for WIMPs physicists must actually search for missing transverse energy (MET) in a collision. The MET can be reconstructed by observing the outgoing particles and jets in a collision based on momentum conservation. This reconstruction is shown in Fig. 1.10. Ultimately, this MET can be used to determine the mass and the new physics processes of the WIMP [24].

One important note is that while we can potentially "see" WIMPs in detectors at colliders, it is impossible to be certain that this WIMP is what makes up the majority

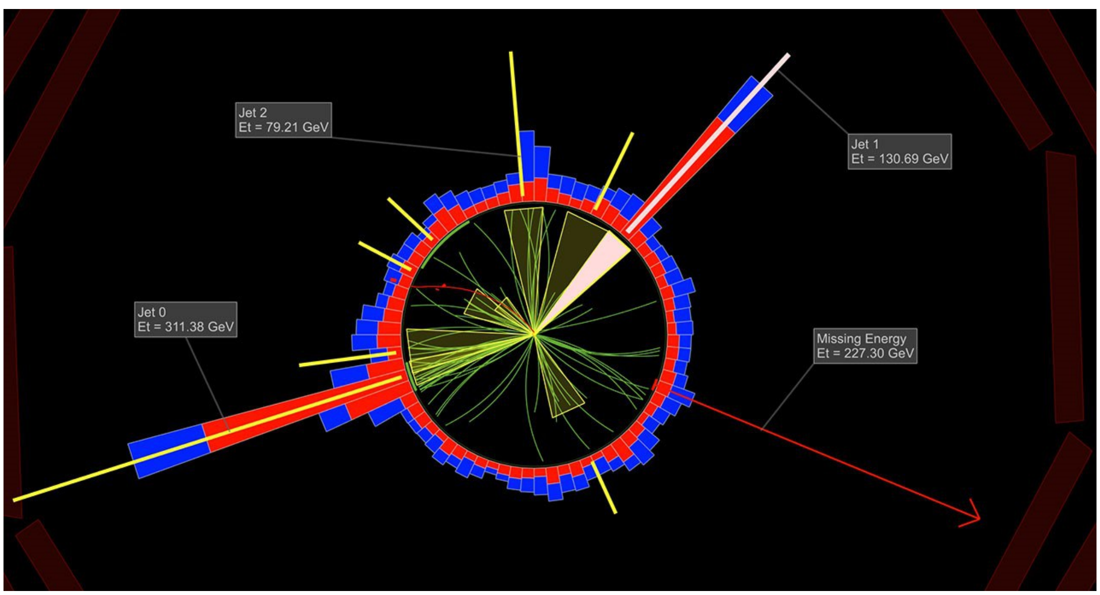

Figure 1.10: An image of a potential WIMP event in the CMS detector at CERN. If a WIMP is present in a collision, momentum would not be conserved after all jets and particles have been accounted for in the collision. Here we can see that after the three jets are reconstructed that there is still a large MET that could potentially be attributed to a WIMP. Image Credit: Matevz Tadel, UC San Diego/CMS.

of the matter in the universe. The same signal would need to be seen in indirect and direct searches as well to make such a confirmation [30].

1.4.3 Direct Detection

In purely theoretical terms, any detector that is sensitive to a potential WIMP interaction could be considered a direct detection dark matter search. At the same time, to try and detect a dark matter signal from a NaI detector in your lab would be preposterous (unless your detector is 250 kg and located deep underground!), the reason being that any of the rare dark matter signals would be drowned out by the countless background events you would also detect. This is why direct detection experiments are typically built deep underground with shielding and low radiation materials and take great care to understand their background as well as they possibly can: if WIMPs are scattering in the detector they want to be able to know.

The goal of direct detection experiments is to detect the scattering of WIMPs off of standard model particles. As mentioned, since these scatters should be extremely rare, it is essential to have the background of the detector used be as low as possible. As a simple example, consider two otherwise identical experiments who both have measured their backgrounds perfectly: experiment A expects a single background event per year while experiment B expects 1,000 background events per year. In the case that both detectors see an excess of ten events in a given year over their background, it should be clear that experiment A can make a very strong claim that they have seen WIMP scatterings whereas experiment B cannot since this excess could very well be a fluctuation from their expected background.

It cannot be emphasized strongly enough how crucial the understanding of background is for direct detection experiments. Returning to the above example, imagine experiment A missed a source of background in their estimate and that their true expected background rate is ten events per year, not one. If they saw the same eleven events as before, they might claim a discovery even though the eleven events are very likely to be a statistical fluctuation of the background.

The most basic models describing WIMPs predict that they are most likely to interact with atomic nuclei (although some predict leptonic interactions [31]). This assumption, along with cosmological evidence that WIMPs are non-relativistic, surprisingly gives way to a fairly straight-forward derivation of the rate of scattering that one could expect for different nuclei, and therefore a complete detector, assuming a given scattering cross-section and mass for the WIMP. For a complete derivation one should refer to Ref. [22] and Ref. [32].

It can be shown that the differential scattering rate is given by [33]

$$\frac{dR}{dE}(E) = \frac{\rho_0}{m_\chi m_A} \int_{v_{\min}(E)}^{v_{\mathrm{esc}}} v f(v) \frac{d\sigma}{dE}(E, v) dv \tag{1.8}$$

where ρ_0 is the local dark matter density, m_χ is the mass of the WIMP, m_A is the mass of the target nucleus, $f(v)$ is the velocity distribution of dark matter locally, v_{min} is the minimum velocity that can produce a recoil of energy E, v_{esc} is the maximum velocity in which WIMPs are still gravitationally bound to the galactic halo, and $\frac{d\sigma}{dE}$ is the differential cross-section of WIMP-nucleon scattering.

As discussed in Sec. 1.4.1, N-body simulations give us a prediction of roughly $0.2 - 0.4\,\frac{\mathrm{GeV}}{\mathrm{cm}^3}$ for the local dark matter density [27]. We will use the standard halo model (SHM), which is standard for dark matter experiments, such that the velocity of WIMPs in the halo follows a Maxwell-Boltzmann distribution. The minimum velocity of a WIMP to transfer an energy E to a nucleus, v_{min}, is found kinematically to be

$$v_{min} = \sqrt{\frac{m_A E}{2\mu^2}}, \quad \mu = \frac{m_A m_\chi}{m_A + m_\chi} \tag{1.9}$$

while astrophysical measurements of the Milky Way estimate the local escape velocity to be $v_{esc} = 533^{+54}_{-41}\,\mathrm{km\,s^{-1}}$ [34]. It is worth noting that while the Maxwell-Boltzmann distribution is the standard, other models of the velocity distribution exist [35].

The particle physics of the WIMPs comes in at the differential cross-section. The most basic WIMP models predict two potential interactions: a spin-independent or spin-dependent. Focusing on the former, the differential cross-section is given by

$$\frac{d\sigma}{dE}(E, v) = \frac{m_A}{2\mu^2 v^2} \sigma_0 F(E)^2 \tag{1.10}$$

where $F(E)$ is nuclear form factor. The nuclear form factor is the Fourier transform of the ground state mass density and is used to correct the zero-momentum transfer cross-section in the case of a momentum transfer. The nuclear form factor can be approximated by

$$F(q) = \frac{3j_1(qR_0)}{qR_0} e^{\frac{-(qs)^2}{2}}, \quad q = \sqrt{2m_A E}, \quad R_0^2 = \left(1.2A^{\frac{1}{3}}\,\text{fm}\right)^2 - 5s^2 \tag{1.11}$$

where q is the momentum transfer in the scatter, R_0 is the approximate nuclear radius, s is the approximate thickness of the nucleus (roughly 1 fm), and j_1 is the spherical Bessel function of the first kind [36].

We can reduce σ_0, the cross-section of an interaction with zero momentum transfer, by accounting for the coupling to the individual nucleons in the following way

$$\sigma_0 = \frac{(Zf_p + (A-Z)f_n)^2}{f_p^2} \frac{\mu^2}{\mu_{\chi p}^2} \sigma_p \tag{1.12}$$

In this equation, f_p and f_n are the WIMP couplings to the proton and neutron, respectively, $\mu_{\chi p}$ is the reduced mass of the WIMP-proton system, and σ_p is the spin-independent cross-section of the WIMP with the proton. We approximate that $f_p \approx f_n$ which allows us to simplify to

$$\sigma_0 \approx A^2 \frac{\mu^2}{\mu_{\chi p}^2} \sigma_p \tag{1.13}$$

All of this can be combined such that we are only dependent on two variables: the mass of the WIMP and its cross-section with a proton.

$$\frac{dR}{dE} = \frac{\rho_0 A^2 \sigma_p}{2m_\chi \mu_{\chi p}^2} F(E)^2 \int_{v_{\min}(E)}^{v_{\text{esc}}} \frac{f(v)}{v} dv \tag{1.14}$$

With the differential scattering rate, we can predict the number of WIMPs of a given cross-section and mass we would expect to scatter in a detector wth a certain target mass, M, in a given time period, T. Notice that, as expected, the larger your detector is and the longer you run, the more likely you are to see a WIMP.

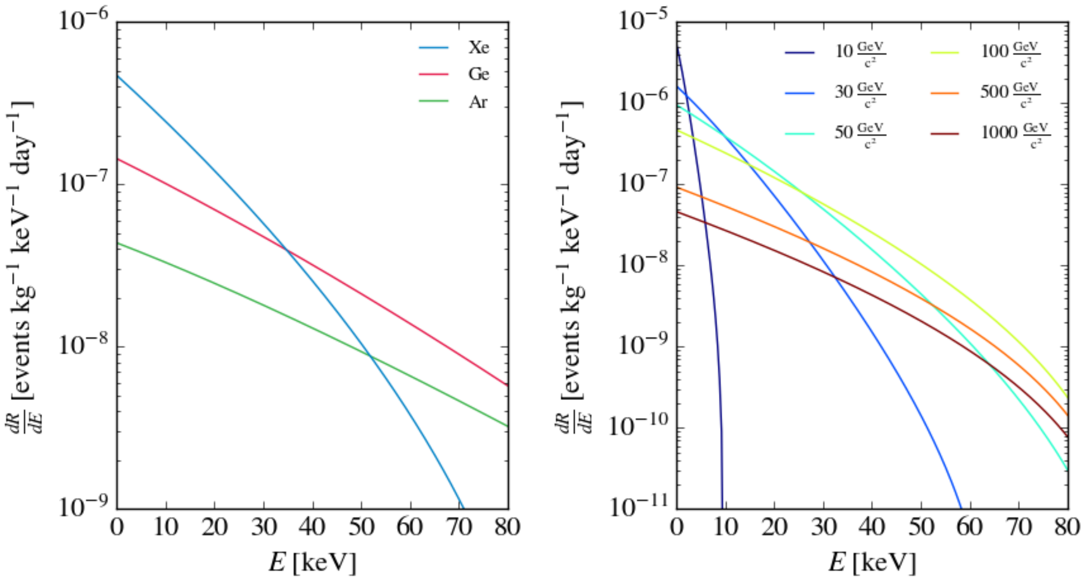

Figure 1.11: On the left are the differential scattering rates for a 100 $^{\mathrm{GeV}}/_{\mathrm{c}^2}$ WIMP with a spin independent cross section of $10^{-47}\,\mathrm{cm}^2$. On the right are the differential recoil spectra for WIMPs scattering with a xenon nuclei with a spin independent cross section of $10^{-47}\,\mathrm{cm}^2$ assuming different WIMP masses.

$$N(\sigma_p, m_\chi) = M\,T \int \frac{dR}{dE} dE \tag{1.15}$$

The differential scattering rates for a few targets and for different WIMP masses can be seen in Fig. 1.11. Notice that xenon, with its very large nucleus, gives a significantly higher scattering rate versus most other targets for a wide range of energies. Also notice that as the mass of the WIMP decreases, the differential scattering rate curve becomes steeper and steeper meaning that low mass WIMPs become increasingly difficult to observe.

1.4.4 Direct Detection Experiments

The field of direct detection experiments is likely best described as diverse. A WIMP interacting in a detector can deposit energy resulting in heat, ionization, or scintillation. Current direct detection experiments leverage all three of these possibilities and many use two of these channels simultaneously to better discriminate types of

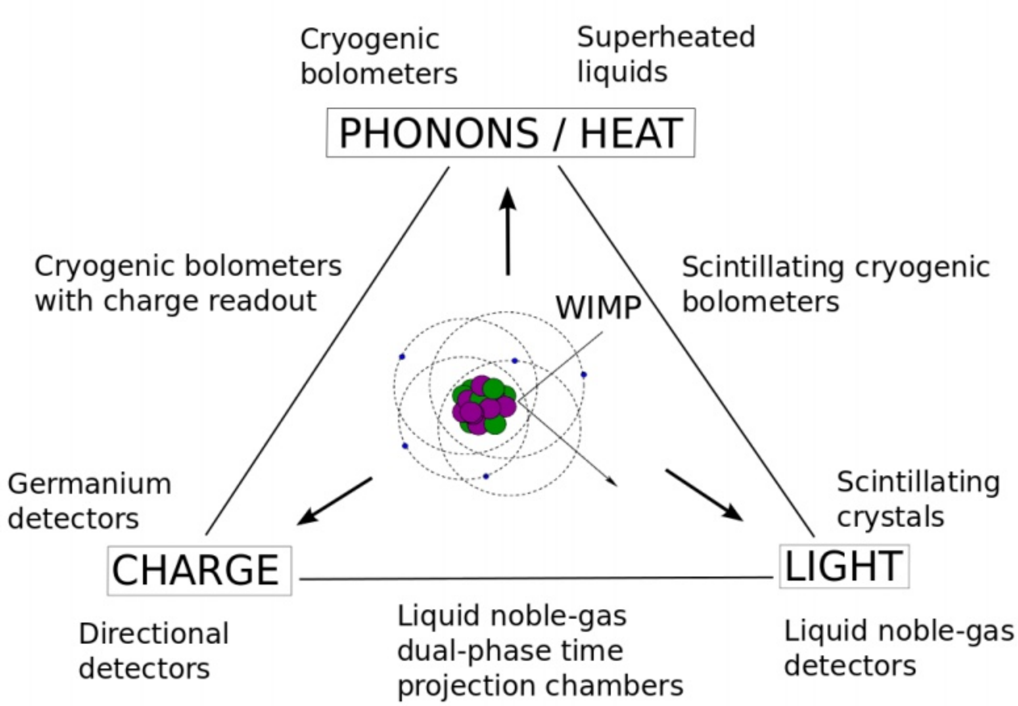

Figure 1.12: A diagram showing the possible observables and observable combinations along with the most common detector types for each. Image courtesy: [33].

interactions (electronic vs. nuclear recoils).

Heat

There are two basic strategies of measuring the heat deposit of potential WIMP interactions that are on opposite sides of the temperature spectrum: cryogenic thermometers and super-heated liquids (bubble chambers). Cryogenic thermometers are detectors cooled down to mK levels that measure the energy deposited by an interaction via the increase in temperature. In recent years, these cryogenic thermometers have been coupled with light and charge detectors in order to discriminate between electronic and nuclear recoils to some extent [37].

Bubble chambers operate by filling a detector with a super-heated liquid that is just below its boiling point. When ionizing radiation enters, it will form bubbles that can be detected by acoustic sensors. One major advantage of bubble chambers is that they are almost completely insensitive to radiation that interacts electronically which is the main source of background for almost all other experiments. The PICO collaboration uses bubble chamber technology to search for dark matter and they currently have the most stringent spin-dependent dark matter limits [38].

Scintillation

Scintillators have proven to be some of the most useful detectors in all of physics. The operating principle is that as radiation pass through a detector, it excites the atoms and molecules in the medium which in turn produce light. In single-channel scintillation experiments, scintillating inorganic crystals, such as NaI, are typically used. Inorganic crystals are typically doped with an additional element, most commonly thallium, to increase their light yield and alter the wavelength to one that is more sensitive to photomultiplier tubes (the devices that are used to convert the light into an electrical signal). The major downside of using an inorganic crystal, however, is that one cannot discriminate between different types of recoils in the detector [33]. The most famous experiment to use an inorganic crystal is the DAMA collaboration, which utilized a 250 kg NaI(Tl) crystal. Since their operation began they have seen a statistically significant annual modulation in their event rate that agrees with predictions of how a dark matter signal would vary over the course of the year according to the standard halo model [39]. Fig. 1.13 shows this annual modulation. However, the claim that the signal is dark matter has been extremely controversial since other experiments have been unable to replicate the results under the assumptions of many models and even an annual modulation test in an alternate detector [40–42].

While many experiments use condensed noble gasses that scintillate, they typically measure both scintillation and ionization in the medium. However, there are some experiments that are hoping to witness a WIMP interaction while only measuring scintillation. XMASS-I, for example, is a detector with an 832 kg liquid xenon target that, like DAMA, employed an annual modulation approach in their search for WIMPs. Unlike DAMA, however, they see no annual modulation in their data [41].

A useful property of condensed noble gasses is that there are usually two states in which the atoms or molecules can be excited into, a singlet and triplet state each with

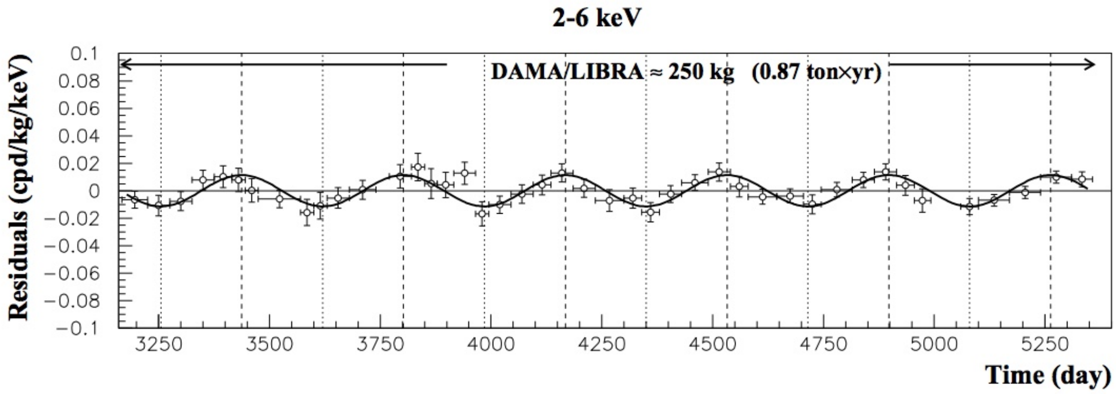

Figure 1.13: The annual modulation seen by the DAMA collaboration. The modulation is statistically significant yet is in contrast to other experiments who fail to see the same signal. Image Credit: [33].

different decay times, and different types of interaction (electronic versus nuclear) will produce each in different fractions. For argon, this difference in lifetime between the states is from less than 6 ns to 1,300 ns [43] meaning that pulse shape discrimination (PSD) is possible, while for xenon the difference is only 4.3 ns to 22 ns meaning that PSD is very difficult. DEAP-3600, a 3600 kg liquid argon detector, uses this pulse shape discrimination technique to identify nuclear recoils in their detector [44].

Ionization

The majority of experiments that used charge as their only channel utilized high-purity germanium detectors. These type of detectors operate by having incoming particles free electrons in a consistent and linear fashion as function of energy. These types of detectors are able to observe interactions at much lower energies than most other detectors, allowing them to probe lower WIMP masses. The most recent of these single-channel HPGe experiments was CoGeNT. In early 2014, CoGeNT announced that they also had seen an annual modulation that matched the standard halo model [45] however this was found to be an error in the estimation of the background [40].

Heat-Scintillation

As mentioned earliers, many of the experiments that use heat as a channel also couple it with another channel. CRESST-II is an example of such an experiment — CREST-II uses a roughly 5 kg target of $CaWO_4$ that is cooled to mK temperatures. The detector also utilizes a small silicon-on-sapphire absorber to measure the scintillation light produced. The addition of this scintillation detector enables the detector to discriminate between electronic recoil background and potential nuclear recoil signals [37].

Heat-Ionization

The HPGe crystals used to detect ionization signals can also be cooled such that measuring heat signals is possible. One example of this procedure is in the EDELWEISS-III experiment. In EDELWEISS-III, 24 800 g HPGe detectors cooled to 18 mK were employed in their search for WIMPs. Again, this combination of channels allows EDELWEISS-III to discriminate electronic from nuclear recoils in their detector [46].

Scintillation-Ionization

While many of the experiments mentioned excel at low mass, none have been as successful as dual-channel scintillation-ionization experiments above masses of approximately 5 GeV. Specifically, dual-phase liquid xenon time projection chambers (TPCs) have led the field in the WIMP search from roughly 5 GeV to 1 TeV for almost a decade. As of this writing, XENON1T, the first ton-scale dual-phase TPC, holds the strongest limit of spin-independent WIMP scattering, as can be seen in Fig. 1.14 [47, 48]. Not only are these detectors capable of a high level discrimination between electronic and nuclear recoils but they are also capable of measuring the position of an interaction in the detector allowing further elimination of background sources. However, one of the major difficulties of these types of experiments is that the response of liquid xenon to low energy electronic and nuclear recoils is not well understood. A great deal of effort has gone into measuring the response of xenon to

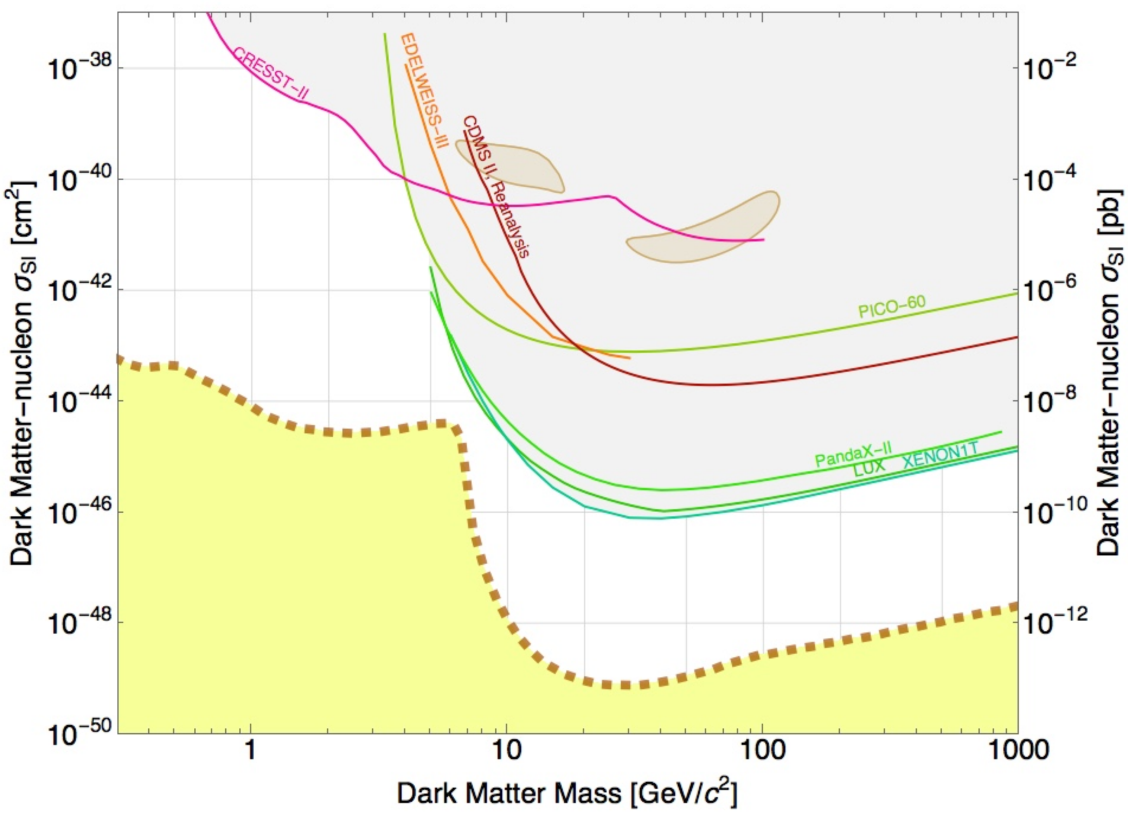

Figure 1.14: Selected spin-independent WIMP limits from selected experiments and the discovery contour from DAMA's annual modulation. The dashed line shown in brown marks the point where neutrinos will become a background source in WIMP searches. Notice that the three liquid xenon dual-phase TPC based experiments (PandaX-II, LUX, and XENON1T) set the strongest limit over a wide range of WIMP masses [38, 46, 47, 49–54].

these low energy interactions and later we will focus on an experiment designed for exactly this purpose.

Chapter 2

Liquid Xenon and Dual-Phase TPCs

This chapter will focus on liquid xenon as a detector medium. In Sec. 2.1 we will discuss the general properties of liquid xenon along with some of the benefits and considerations of these properties. In Sec. 2.2 we will discuss how charged particles in xenon deposit their energy. In Sec. 2.3 we will discuss the production of observable light and charge from electron recoils while in Sec. 2.4 we will discuss observable production from elastic nuclear recoils. Finally, in Sec. 2.5, we will discuss how these observables are detected in dual-phase xenon time projection chambers.

2.1 General Properties

Xenon, with an atomic number of 54, is a noble gas meaning that it has a full valence electron shell. Because of the full valence shell, xenon is very unlikely to interact chemically with other elements and molecules. Xenon is also the heaviest noble gas that is, for practical purposes, naturally non-radioactive. ^{136}Xe, with a natural abundance of 8.857%, has been show to undergo double beta decay with a half-life of $2.165 \cdot 10^{21}$ years so strictly speaking natural xenon is radioactive although this process is extremely rare and has little relevance for even low background dark matter experiments [55].

While natural xenon is not radioactive, it is actually possible to excite xenon nuclei such that they decay and emit gamma rays. None of these excited states have very long lifetimes that would cause issues for low background experiments but two of these neutron activated states (^{131m}Xe and ^{129m}Xe which decay emitting 164 keV and 236 keV photons, respectively) have half-lives on the order of ten days. This half-life could potentially be very useful in the calibration of large detectors since over this period of time the excited states would be approximately uniformly distributed inside of a detector [56].

Xenon is extracted from the atmosphere as a byproduct of the separation of oxygen and nitrogen. Once the oxygen is separated, it will contain trace amounts of krypton and xenon that can be separated out further by distillation or adsorption. The xenon that is purchased commercially typically will have a final Kr/Xe ratio of $\sim 10^{-6} - 10^{-9}\frac{\text{mol}}{\text{mol}}$. Natural krypton is not radioactive on a relevant time scale but ^{85}Kr, which is released into the atmosphere via nuclear fuel reprocessing and nuclear weapons tests, beta decays with a mean energy of 251 keV and with a half-life of roughly 10.8 years [57]. So while natural xenon is not radioactive, the process of extracting xenon from the atmosphere does leave a radioactive isotope that could be a potential source of background for dark matter experiments. Significant effort has gone into reducing the Kr/Xe levels to reduce this background as much as possible. In XENON1T, the lowest level to date was achieved with a natural krypton to xenon ratio of less than 200 ppq (1 ppq $= 10^{-15}\frac{\text{mol}}{\text{mol}}$) [58].

Dual-phase xenon experiments typically operate at roughly 2–3 atm, which translates to a boiling point of roughly 180 K (-93.2° C). The density of liquid xenon (LXe) at this temperature is roughly 2.84 $^{\text{g}}/_{\text{cm}^3}$ which is significantly higher than all of the other noble elements, with the exception of radon [60]. The high density of LXe is partly responsible for its high electronic stopping power, which will be discussed further in the next section.

Isotope	Abundance	Spin	Half-life	Decay Mode
^{124}Xe	0.095%	0	$> 1.6 \cdot 10^{14}$ y	$2\nu\beta^+\beta^+$ [1]
^{126}Xe	0.089%	0	$4.7 - 12 \cdot 10^{25}$ y	$2\nu\beta^-\beta^-$ [1]
^{128}Xe	1.910%	0	Stable	-
^{129}Xe	16.400%	$1/2$	Stable	-
^{130}Xe	4.071%	0	Stable	-
^{131}Xe	21.232%	$3/2$	Stable	-
^{132}Xe	26.909%	0	Stable	-
^{134}Xe	10.436%	0	$> 5.8 \cdot 10^{22}$ y	$2\nu\beta^-\beta^-$ [1]
^{136}Xe	8.857%	0	$2.2 \cdot 10^{21}$ y	$2\nu\beta^-\beta^-$

Table 2.1: Abundances, half-lives, and decay modes of various xenon isotopes. Note that ^{136}Xe is the only isotope whose decay has been measured. Half-life data: [59].

2.2 Energy Deposition of Charged Particles in Liquid Xenon

Both nuclear and electronic recoils, which will be discussed in the following sections, ultimately result in a charged particles traversing the LXe - in the case of an electronic recoil the resulting charged particle is an electron and in the case of nuclear recoils it is the xenon nucleus. Given the high density and atomic number of xenon, the electronic stopping power is large for both electrons and xenon ions ($\sim 1-30\,{}^{\mathrm{keV}}/_{\mu\mathrm{m}}$). This means that the tracks of low energy electronic and nuclear recoils will be very small and approximately point-like [61].

In liquid xenon (and other noble liquids), scintillation light is produced via the excitation of atomic electrons and the ionization and subsequent recombination of free electrons and ions. The excitation scintillation process is shown in Eqn. 2.1 and the ionization scintillation process is shown in Eqn. 2.2.

$$\begin{gathered} \mathrm{Xe}^* + \mathrm{Xe} + \mathrm{Xe} \rightarrow \mathrm{Xe}^*{}_2 + \mathrm{Xe}, \\ \mathrm{Xe}^*{}_2 \rightarrow 2\mathrm{Xe} + h\nu \end{gathered} \tag{2.1}$$

[1]This decay is predicted but has not yet been observed.

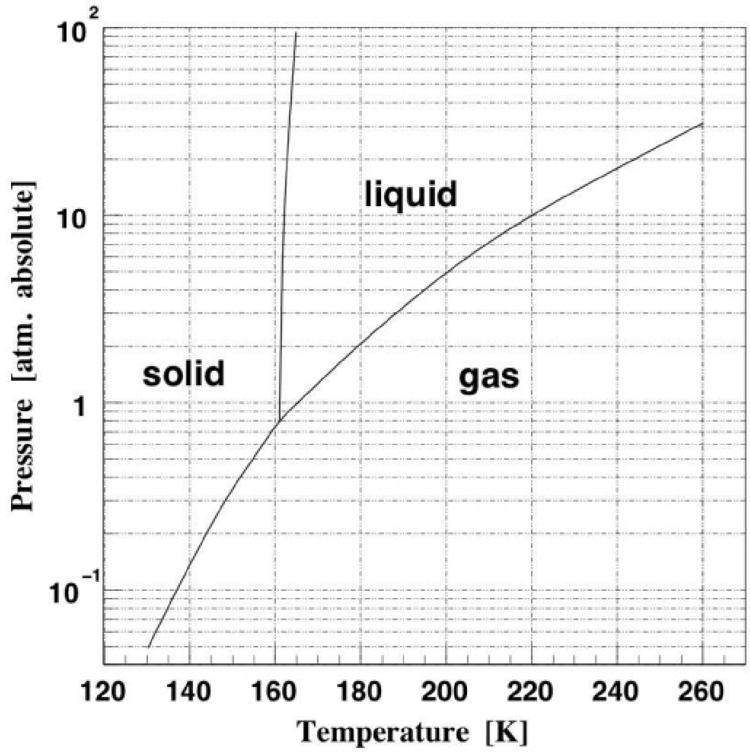

Figure 2.1: The phase diagram for xenon. Dual-phase xenon TPCs typically operate in the range of 2–3 atm.

$$\begin{aligned}
\mathrm{Xe}^{+} + \mathrm{Xe} &\rightarrow \mathrm{Xe}_2^{+}, \\
\mathrm{Xe}_2^{+} + e^{-} &\rightarrow \mathrm{Xe}^{**} + \mathrm{Xe}, \\
\mathrm{Xe}^{**} &\rightarrow \mathrm{Xe}^{*} + \mathrm{heat}, \\
\mathrm{Xe}^{*} + \mathrm{Xe} + \mathrm{Xe} &\rightarrow \mathrm{Xe}^{*}{}_2 + \mathrm{Xe}, \\
\mathrm{Xe}^{*}{}_2 &\rightarrow 2\mathrm{Xe} + h\nu
\end{aligned} \tag{2.2}$$

The excitation process proceeds when an an atomic electron in xenon is excited (the excited xenon is referred to as an *exciton*) and the excited atom forms a dimer with another xenon atom, which is called an *excimer*. This excited excimer can be formed in either the singlet state (spin of excited electron anti-parallel to electron originally sharing state) or triplet state (spin of excited electron parallel to electron originally sharing state). The excimers in the singlet and triplet states each have their own characteristic lifetimes (roughly 4 ns and 22 ns)[2] and decay into xenon atoms and a 178 nm photon (the photon falls in UV portion of the spectrum) [62, 63].

The ionization process begins when a charged particle ionizes a xenon atom, leaving singly-ionized xenon and a free electron. The singly-ionized xenon atom can then form an ionized dimer and subsequent excited xenon state. This excited xenon state leads to an excimer through non-radiative heat loss. The excimer produces scintillation light in the manner described above.

Implicit in the ionization process outlined above is the assumption that the electron freed during ionization recombines with the singly-ionized dimer. However, in the presence of an electric field, this recombination can be reduced such that a charge signal can also be read out in addition to the scintillation signal. Incomplete recombination can also occur at zero electric field and these electrons are called *escape electrons* (although you cannot extract the charge signal without an applied electric field) [63].

It is important to note that while these electronic excitation and ionization mechanisms are dominant for electronic recoils, the energy deposition for nuclear recoils is split between these and atomic motion. This distinction is extremely important - the energy given to electrons in a recoil cannot cause atomic motion however atomic motion, if sufficiently slow, will not be able to cause excitation or ionization in other atoms and hence some energy is lost. This effect was first discussed by Lindhard in 1963 [64] and the effort to quantify this effect continues today and in this work. This effect will henceforth be referred to as nuclear quenching.

A second form of quenching has been observed in high linear energy transfer (LET) interactions, specifically with α scatters in xenon (which will not be discussed in detail) and high energy nuclear recoils. This quenching is called biexcitonic quenching and is the result of two excitons colliding to produce an electron-ion pair as shown in Eqn. 2.3.

[2] In xenon the difference in lifetimes of the singlet and triplet states is fairly small but for argon the singlet lifetime is 7 ns while the triplet lifetime is 1.3 μs [43]!

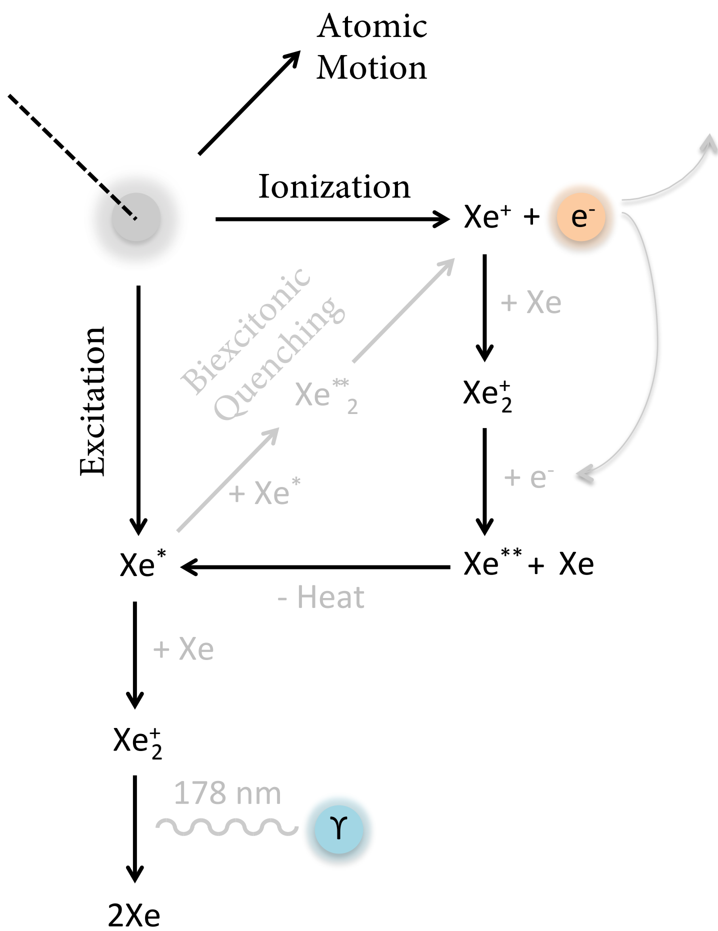

Figure 2.2: A diagram showing the modes in which charged particles may lose energy in liquid xenon. Note that when an electric field is applied, the electron freed during ionization can be extracted such that it can be measured.

$$\mathrm{Xe}^* + \mathrm{Xe}^* \rightarrow \mathrm{Xe} + \mathrm{Xe}^+ + e^- \tag{2.3}$$

Since this form of electronic quenching requires the collision of two excitons, it is expected that the track density ultimately determines the level of quenching [65].

A diagram showing all of the mentioned energy deposition methods for charged particles is shown in Fig. 2.2.

2.3 Electronic Recoils in Liquid Xenon

In this section, we will discuss the sources of electronic recoils in liquid xenon, their properties, and how they result in detectable observables. For dual-phase LXe TPCs (which we will focus on in more detail later) searching for "standard" WIMPs, electronic recoils constitute the background. With a precise understanding of what causes electronic recoils and how they interact in LXe, we can better discriminate between electronic recoils and potential signals that are expected to interact via nuclear recoils. Additionally, if WIMPs do interact with atomic electrons rather than the nucleus, a precise understanding of the electronic recoil background would be crucial for a discovery.

2.3.1 Sources of Electronic Recoils

There are two main sources of energetic electrons in liquid xenon: (1) beta decays from contaminants inside of a detector and (2) photons interacting through matter via photoelectric absorption, Compton scattering, or pair production. In either case, the resulting energetic electron creates a track through the xenon, mainly losing its energy from inelastic collisions with atomic electrons. In standard WIMP hypotheses, WIMPs are expected to interact with the atomic nucleus, however there are certain theories of WIMPs that allow interactions between a WIMP and atomic electrons that would result in an electronic recoil.

Beta Decays

While there are both β^- and β^+ decays, we will focus on β^- decays since they are relevant to WIMP searches. β^- decay is a radioactive decay in which a neutron is converted to a proton inside of the nucleus and a subsequent electron and anti-electron neutrino are emitted. This type of decay is made possible by the weak force which allows a quark to change its type via a W boson and an electron and anti-neutrino (positron and neutrino) pair [66].

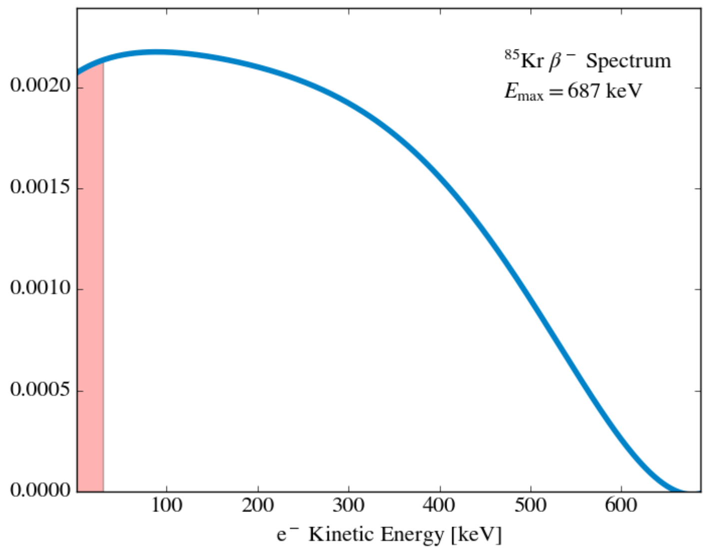

Figure 2.3: The kinetic energy spectrum of electrons resulting from the β^- decay of ^{85}Kr [67]. Note that roughly 6.5% of decays are below 30 keV (shaded red region) which puts them inside the energy region of interest of WIMP searches.

While the maximum energy of the energetic electron in the decay is fixed, because an anti-neutrino is also emitted in β^- decay, the energy spectra of the electron is continuous. This continuous energy spectrum is what makes long-lived β^- emitters very dangerous potential sources of background - they can, with non-negligible probabilities, produce electrons with energies of interest for WIMP detection ($\lesssim 30$ keV). The energy spectrum for ^{83}Kr is shown in Fig. 2.3.

In liquid xenon based detectors, the two biggest sources of background beta decays are from ^{85}Kr and ^{214}Pb, which comes from the ^{222}Rn decay chain [47]. Even though certain atoms that β^- decay prove to be a background that must be carefully reduced, others have proven to be extremely useful for detector calibrations. ^{212}Pb, from the decay chain of ^{220}Rn, has proven useful for calibrations since approximately 10% of electrons have an energy less than 30 keV (the maximum energy is 570 keV) [68]. Perhaps even more exciting for the low energy calibrations of electronic recoils is the use of tritium, which has a maximum energy of only 18.6 keV [69, 70]! [3]

Photons

Another source of electronic recoils in LXe comes from photons. Photons, via photoelectric absorption, Compton scattering, or pair production, can create energetic electrons inside of a detector. While pair production is not relevant in the energy range of interest, photoelectric absorption is one of the most tried and tested calibration tools for LXe (and other detectors) and electrons from Compton scatters can make up part of the background in WIMP searches since the energy of the electron can be arbitrarily low.

Photoelectric absorption is the process by which a photon is absorbed by an atom from which an electron is subsequently ejected (typically from the K shell). This implies that the energy of the ejected electron is equal to the energy of the photon minus the binding energy. However, the newly ionized atom will have a free electron bind with it, usually on a very short time scale, and an X-ray or auger electron will be emitted [71]. Therefore the energy detected from photoelectric absorption will be very close to the initial energy of the photon. Photoelectric absorption is the dominant mode of interaction up to a few hundred keV in most media, including xenon as can be seen in Fig. 2.4.

Compton scattering is the process by which a photon interacts with an atomic electron resulting in the deflection of the photon at a specific angle and a transfer of energy to the electron. The angle of the scattering completely describes the energy transferred to the electron. Compton scattering is the dominant mode of interaction from a few hundred keV to a few MeV in most media, including xenon as can be seen in Fig. 2.4.

Fig. 2.4 shows the mass attenuation coefficient of photons in LXe and the individual contributions of each process. Because of xenon's high atomic number, all

[3]Molecular tritium (T_2) cannot be used because it adsorbs to surfaces very easily and the half-life of T_2 is 12.3 years. Instead, tritiated methane (CH_3T) is used since this will not adsorb and can be easily removed.

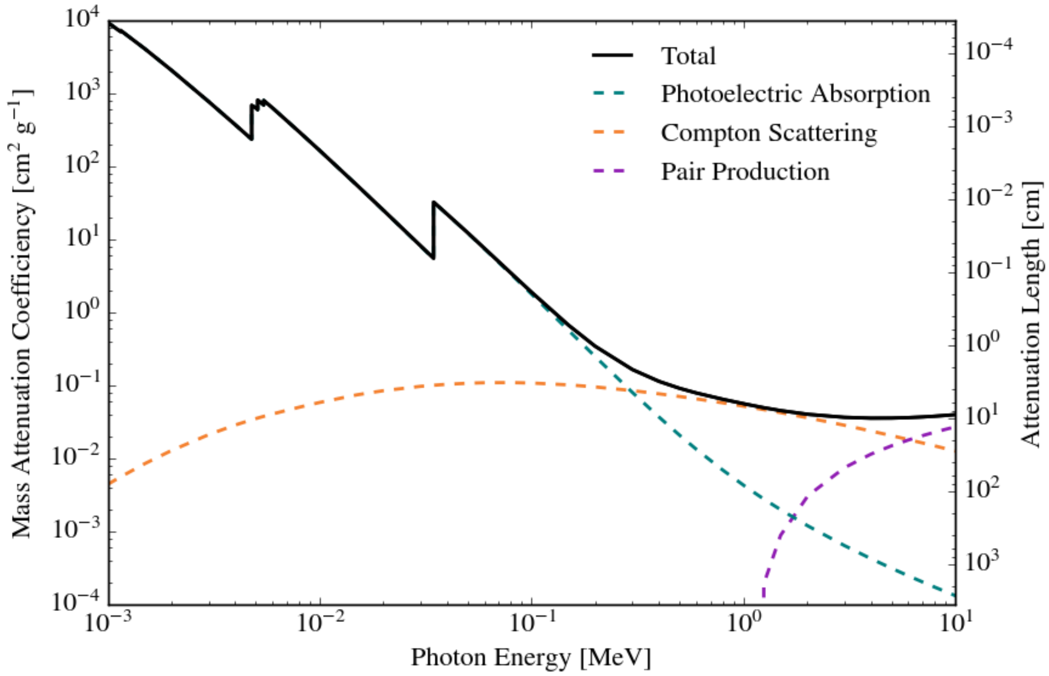

Figure 2.4: The mass attenuation coefficient and the attenuation lengths for photons of different energies in liquid xenon [72].

processes have very high attenuation coefficients. This is valuable for background reduction since low energy photons are absorbed at the very edge of the detector (since their attenuation length is < 1 cm) although it does make calibration with external gamma ray sources very difficult for large detectors.[4] Photons with an energy of a few hundred keV to a few MeV are most likely to Compton scatter and not be absorbed and have an attenuation length on the order of several centimeters which means that they will contribute to the background of LXe detectors at some level.

Neutrons

Neutrons can interact in liquid xenon mainly through three mechanisms: radiative absorption and inelastic scattering, which result in electronic interaction in the medium, and elastic scattering, which ultimately results in a nuclear recoil and will be discussed

[4]This is the reason why many large scale LXe detectors are calibrated using internal sources now such as the beta emitters mentioned earlier and metastable activated xenon.

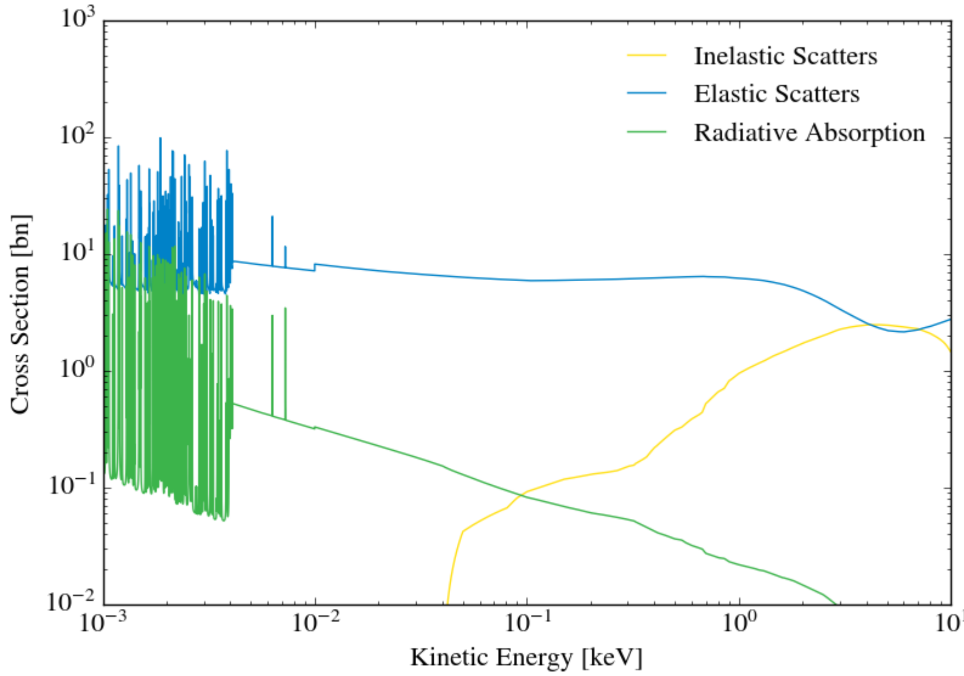

Figure 2.5: The cross-sections of the three main interaction modes of neutrons in liquid xenon. Note that elastic scattering is the dominant process for almost all energies in the range shown. The data for each isotope of xenon is from Ref. [73] and the figure shows the cross-sections weighted by abundance of each isotope in natural xenon.

in Sec. 2.4. The cross-sections of each of these mechanisms for xenon can be seen in Fig. 2.5. Note that for almost all energies between 1 keV – 10 MeV that elastic scattering is the dominant process.

Radiative absorption is the absorption of neutrons by a nucleus. The nucleus thus increases by one in mass number with atomic number staying the same. Fortunately, since the isotopes of xenon that could be produced are not radioactive, with the exception of ^{133}Xe and ^{135}Xe, this process produces very little background. ^{133}Xe and ^{135}Xe both result in short β^- chains and will therefore result in electronic recoils inside of a detector. With this said, for the neutron energies of background and calibrations in liquid xenon WIMP detectors, radiative absorption is largely irrelevant.

Inelastic scattering is the process by which a particle interacts with the atomic nucleus and kinetic energy is lost due to the excitation of the nucleus. The excitation of the nucleus, also called *activation*, is then followed by the nucleus decaying from this excited state back down to a stable state through the emission of a particle. For xenon, there are two inelastic collisions of note: an inelastic scattering with ^{129}Xe or ^{131}Xe. A neutron scattering inelastically with ^{129}Xe can result in nucleus being in an excited state with a 0.96 ns half-life that decays into gamma ray at an energy of approximately 40 keV or in an excited metastable state with a half-life of 8.8 days that results in a 197 keV photon followed by a 40 keV photon (the 40 keV photon is from the same very short lived state that the metastable state decays into) [74]. A neutron scattering inelastically with ^{131}Xe can result in the nucleus being in a metastable state with a half-life of 11.84 days that decays emitting a 164 keV photon [75]. While these processes are not relevant for background considerations during a WIMP search, they are very useful when calibrating a detector since they each result in electronic recoils at a low and fixed energy.

There are three major sources of neutrons in dark matter experiments. The first major source is from heavy elements in various detector components decaying via spontaneous fission resulting in neutrons with energies typically from 1 – 10 MeV. Neutrons also come from high-energy muons interacting with the rock and materials around the detector. Finally, neutrons can be produced artificially using a neutron generator (typically either through a deuterium-deuterium reaction or deuterium-tritium reaction). The first two sources of neutrons make up background in dark matter searches while the third source of neutrons is used to calibrate detectors (for both electronic and nuclear recoils).

Neutrinos

Neutrinos can elastically scatter with electrons either via charged-current (exchange of W boson) or neutral-current (exchange of Z boson) interactions. For electronic recoils, the main sources of neutrinos are from initial deuterium production and ^{7}Be reactions inside the sun (roughly 92% and 7% of the neutrino background, respectively) [76]. Like electronic recoils from beta decays, the kinetic energy of the recoiling electron will follow a spectrum where only very low energies ($\lesssim 30$ keV) are relevant. Unlike

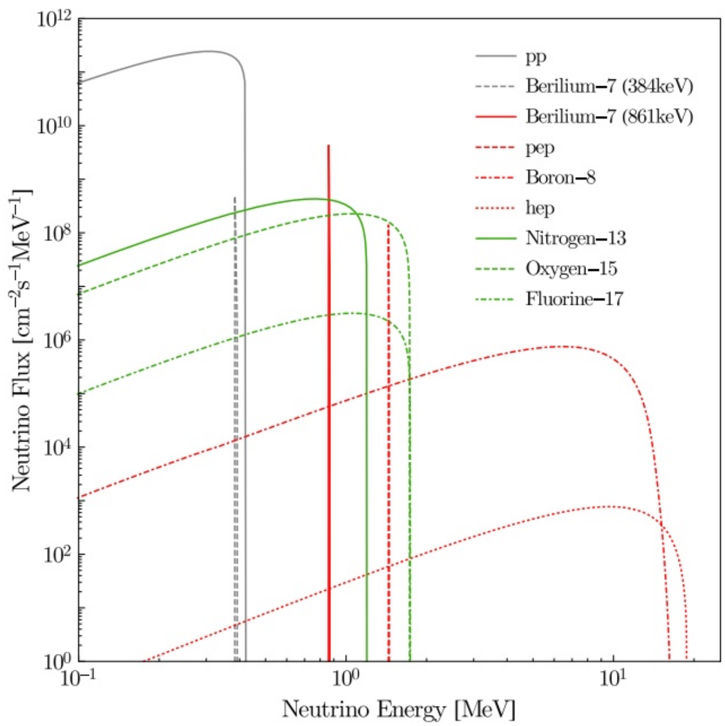

Figure 2.6: Solar neutrino fluxes from different processes assuming the BS05(OP) standard solar model. Image Credit: [77].

other sources of electronic recoils, the solar neutrino background cannot be reduced.

2.3.2 Observables Production for Electronic Recoils

In Sec. 2.2, we discussed the modes by which charged particles deposit energy in LXe. We will now quantify these observables production methods for electronic recoils under the assumption of an applied electric field.

As mentioned in Sec. 2.2, electronic recoils result in either excitation or the creation of electron-ion pairs. Assuming the recoils occur in the presence of an electric field, we do not need to be concerned about quenching with respect to escape electrons (since these can be extracted by the electric field and ultimately measured). Additionally, electronic recoils have relatively sparse tracks (as can be seen by their low stopping power in liquid xenon) [61] so it is expected that biexcitonic quenching will not play a large role in observables production.

Since there are no major forms of quenching, we can completely separate the energy deposited in the electronic recoil into excitons and electron-ion pairs. Typically the total number of quanta (excitons and electron-ion pairs) is used to describe this relationship — specifically, the average energy required to produce a single quanta. For xenon, this value is $W = 13.7 \pm 0.2\,\mathrm{eV}$ [78] and the relationship is given by Eqn. 2.4.

$$N_q = \frac{\mathrm{E_{ER}}}{W} = N_{\mathrm{ex}} + N_{\mathrm{ion}} \tag{2.4}$$

This relationship, while looking very simple, turns out to be extremely useful for calibrations in dual-phase xenon TPCs, as we will discuss in later chapters. The breakdown of excitons to electron-ion pairs is simply described by the ratio of the two quantities such that we can define probabilities of a given quanta being an exciton or electron-ion pair.

$$p_{\mathrm{ion}} = \frac{1}{1 + \frac{N_{\mathrm{ex}}}{N_{\mathrm{ion}}}}, \quad p_{\mathrm{ex}} = 1 - p_{\mathrm{ion}} \tag{2.5}$$

The exciton-to-ion ratio, $\frac{N_{\mathrm{ex}}}{N_{\mathrm{ion}}}$, has been theoretically calculated to be 0.06 for sub-MeV electronic recoils [79] however measurements and theoretical predictions have also suggested a value of 0.20 ± 0.13 [63, 80].

As mentioned previously, electron-ion pairs have a finite probability of recombining to form excitons and eventually producing a scintillation signal (as opposed to a charge signal). While in the past this recombination probability was modelled using Birks' saturation law [81] for large tracks and the Thomas-Imel model [82] (which will be discussed in more detail for nuclear recoils) for short tracks, recently a great deal of work has gone into directly measuring recombination in liquid xenon and its potential fluctuations without the assumption of a model [69, 70]. Recombination is simply inserted to the model of observables production as shown in Eqn. 2.6.

$$N_{\mathrm{ex}} \leftarrow N_{\mathrm{ex}} + rN_{\mathrm{ion}}, \quad N_{\mathrm{ion}} \leftarrow (1-r)N_{\mathrm{ion}} \tag{2.6}$$

Following recombination in electronic recoils, these excitons and electron-ion pairs directly translate into the number of photons and electrons that are observable.

$$N_\gamma = N_{ex}, \quad N_e = N_{ion} \tag{2.7}$$

2.4 Nuclear Recoils in Liquid Xenon

It is expected that WIMPs could potentially dissipate energy in xenon via elastic nuclear recoils so understanding these type of interactions is of crucial importance for WIMP direct detection experiments. In this section, we will discuss the sources of nuclear recoils in liquid xenon based WIMP searches (besides potential WIMPs) and the observables production process for elastic nuclear recoils, which is substantially more complicated due to the nuclear and electronic quenching first mentioned in Sec. 2.2.

2.4.1 Sources of Nuclear Recoils

The two sources of nuclear recoils in liquid xenon based WIMP searches, besides potential WIMPs, are neutrons and neutrinos. While neutrons are, as one would expect, the main background and calibration source in liquid xenon based WIMP searches, neutrinos are no longer negligible and, as detectors become more and more sensitive to lower cross-sections, will soon comprise an irreducible background of elastic nuclear recoils in detectors. Understanding the sources of nuclear recoils in liquid xenon based WIMP direct detection experiments is very important since an underestimation of the background could lead to potential claims of a false WIMP signal since interactions would be indistinguishable on an event-by-event basis.

Neutrons

Electronic recoils from neutron scattering were discussed in Sec. 2.3 — in this section we will focus on nuclear recoils from elastic scattering. Elastic scattering is the process by which a particle interacts with the atomic nucleus and kinetic energy is conserved. The recoiling nucleus then deposits its energy in the medium which can ultimately be detected. Particles scattering elastically with nuclei is also called a nuclear recoil. Of course, this process is not unique to neutrons but is the main mode of interaction for many massive particles (and hopefully WIMPs).

Each of the sources of neutrons mentioned in Sec. 2.3, spontaneous fission of heavy materials, high-energy muons, and artificially generated muons, can also result in nuclear recoils.

Neutrinos

Neutrinos can interact with both electrons, as discussed in Sec. 2.3, and atomic nuclei, via coherent neutrino-nucleon scattering (CNNS). The maximum energy of a recoiling nucleus is given by $E_{\mathrm{r}}^{\mathrm{max}} = \frac{2E_\nu^2}{m_N+2E_\nu}$, where m_N is the mass of the nucleus and E_ν is the energy of the neutrino. This implies that neutrinos must have energies on the order of 10 MeV to cause nuclear recoils on the order of 1 keV. Therefore, high energy neutrino sources like ^{8}B in the sun as well as neutrinos from supernovae and the atmosphere will contribute the most to the CNNS background in dark matter experiments.

2.4.2 Observables Production for Nuclear Recoils

We will now discuss the details of the observables production process for nuclear recoils that was generally outlined in Sec. 2.2. Like electronic recoils, nuclear recoils can lead to the excitation or ionization of other xenon atoms. However, unlike energetic electrons in liquid xenon, recoiling xenon atoms will also interact with other xenon nuclei. This distinction is extremely important since energy can effectively be "lost" if the energy transferred during a collision is too low to cause excitation or ionization.

Lindhard proposed a theory to describe this nuclear queching in Ref. [64]. To describe the quenching of signals due to atomic motion, it is standard to work with the dimensionless energy given in Eqn. 2.8.

$$\epsilon = 11.5 \left(\frac{E}{\mathrm{keV}}\right) Z^{-7/3} \tag{2.8}$$

Lindhard showed that at low velocities ($v < v_F$) the stopping power of a heavy ion in a medium is approximately given $S_e = k\epsilon^{1/2}$, where k is a proportionality constant, assuming the Thomas-Fermi screening model. Under the same assumptions, it can be shown that $k = 0.133Z^{2/3}A^{-1/2}$, which would give $k \approx 0.165$ for xenon, although in his original paper Lindhard names the calculation of the proportionality factor as the largest source of uncertainty in the stopping power. Shown in Eqn. 2.9 is Lindhard's semi-empirical numerical solution for the fraction of the total energy that goes to electronic interactions for recoiling atoms.

$$L(\epsilon) = \frac{kg(\epsilon)}{1 + kg(\epsilon)}, \quad g(\epsilon) = 3\epsilon^{0.15} + 0.7\epsilon^{0.6} + \epsilon \tag{2.9}$$

Note that $g(\epsilon)$ is not derived from first principles but is a fit to Lindhard's numerical solution from $\epsilon = 0.001 - 100$ (roughly 1 keV – 100 MeV nuclear recoils for xenon).

Similar to observables production in electronic recoils, we assume that all energy that goes towards electronic interactions is converted into excitons and ions by way of the W value as is shown in Eqn. 2.10.

$$N_q = \frac{L(E)E_{\mathrm{NR}}}{W} = N_{\mathrm{ex}} + N_{\mathrm{ion}} \tag{2.10}$$

As with electronic recoils, the split into excitons and ions can be defined by a single parameter, $\frac{N_{\mathrm{ex}}}{N_{\mathrm{ion}}}$.

$$p_{\mathrm{ion}} = \frac{1}{1 + \frac{N_{\mathrm{ex}}}{N_{\mathrm{ion}}}}, \quad p_{\mathrm{ex}} = 1 - p_{\mathrm{ion}} \tag{2.11}$$

Unlike electronic recoils, however, it is expected that $\frac{N_{\mathrm{ex}}}{N_{\mathrm{ion}}} \approx 1$ for nuclear recoils [83–85].

RIVAL (Recoiling Ions in Various Atomic Liquids) simulations show that nuclear recoils, unlike electronic recoils, lose the majority of their energy in a large number of secondary tracks and have a short track size relative to electronic recoils. With short tracks and with applied electric fields we can use the Thomas-Imel recombination model to describe the recombination of electrons and ions into excitons shown in Eqn. 2.2 [78]. The Thomas-Imel box model [82] begins by using the modified diffusion equation presented by Jaffe [86] with the assumptions that Coulomb forces are negligible, due to the high coefficient of polarization for xenon. Jaffe's model is described by Eqn. 2.12.

$$\frac{\partial N_\pm}{\partial t} = \mp u_\pm \boldsymbol{E} \cdot \boldsymbol{\nabla} N_\pm + D_\pm \nabla^2 N_\pm - \alpha N_+ N_- \tag{2.12}$$

In Eqn. 2.12 $N_\pm$ are the ion and electron charge distributions, $u_\pm$ are the ion and electron mobilities, and α is the recombination constant. Thomas and Imel improved upon this model by making appropriate approximations for liquid xenon and argon: the diffusion rate is very small and ion drift is much slower than electron drift (3 – 5 orders of magnitude). These simplifications lead to the set of equations 2.13.

$$\begin{aligned} \frac{\partial N_+}{\partial t} &= -\alpha N_+ N_- \\ \frac{\partial N_-}{\partial t} &= u_- E \frac{\partial N_-}{\partial z} - \alpha N_+ N_- \end{aligned} \tag{2.13}$$

Assuming that the electron-ion pairs are isolated, that the initial distribution of ions and electrons uniformly populates a box of dimension a, and that N_{ion} electron-ion pairs initially fill the box, we can solve equations 2.13 to find the probability of recombination.

$$r = 1 - \frac{\ln(1 + N_{ion}\sigma)}{N_{ion}\sigma}, \quad \sigma = \frac{\alpha}{4a^2 \mu_- E} \tag{2.14}$$

We redefine the number of excitons and electron-ion pairs following recombination in the same way as with electronic recoils.

$$N_{\text{ex}} \leftarrow N_{\text{ex}} + rN_{\text{ion}}, \quad N_{\text{ion}} \leftarrow (1 - r)N_{\text{ion}} \tag{2.15}$$

Since nuclear recoils result in smaller and more dense tracks, we must also account for biexcitonic quenching. Biexcitonic quenching occurs by the process outlined in Eqn. 2.3: two excitons collide ultimately leading to the formation of a single electron-ion pair. This process effectively reduces the two potential photons to a single observable photon. This electronic queching is typically parameterized using the quenching term from Birks' saturation law, as shown in Eqn. 2.16, since one would expect that the density of excitons in a track to be proportional to the electronic stopping power [87–89].

$$f_B = \frac{1}{1+\eta\frac{dE}{dx}} = \frac{1}{1+\eta k\epsilon^{\,-\,1/2}} \tag{2.16}$$

This quenching ultimately reduces the number of photons that will be observable in a given interaction, as shown in Eqn. 2.17.

$$N_\gamma = N_{ex} f_B, \;\; N_e = N_{ion} \tag{2.17}$$

2.5 Dual-Phase Time Projection Chambers

Having discussed how different types of particles deposit their energy in liquid xenon, we can now discuss dual-phase xenon time projection chambers (TPCs), the leading detector type in the search for WIMPs, and how they identify interaction types and reconstruct the position and energy of interactions in a TPC.

2.5.1 Operating Principle

On an interaction-by-interaction basis, the goal of dual-phase xenon TPC is threefold: determine the type of the interaction (nuclear or electronic recoil), determine the energy of the interaction, and determine the position of the interaction. While we will discuss in more detail how each of these goals is achieved in a TPC, it is important to understand how the observables are extracted from the liquid xenon.

For both nuclear and electronic recoils, an interaction in the liquid xenon with an applied electric field results in both photons and free electrons. The number of photons are measured by using photomultipler tube (PMT) arrays at the top and bottom of the detector. These PMTs convert the light signal into a proportional charge signal that can be read by a standard digitizer. This prompt scintillation signal is referred to as the S1 of the interaction. The electric field that is applied vertically in the detector is used to extract the free electrons from the interaction site and to the liquid-gas boundary in the detector. An additional electric field is applied to extract the electrons from the liquid and to accelerate the electrons through the gas, exciting xenon atoms that lead to secondary scintillation photons in the process. This process occurs at a time directly related to the depth of the interaction in the liquid. This secondary scintillation process, which is proportional to the number of electrons extracted from the interaction site, is referred to as the S2 of the interaction. This entire process is depicted in Fig. 2.7 and will be discussed in significantly more detail throughout the remainder of this chapter.

Reconstructing Interaction Type

Since the most basic function of these TPCs is to search for WIMPs via elastic nuclear recoils, it becomes crucially important to be able say what is likely background (electronic recoils) and what is a potential signal (nuclear recoils). Without this type of discrimination, searches are limited to counting techniques like those discussed in the first chapter. Since the electronic recoil background rate is typically several orders of magnitudes larger than the nuclear recoil background, an experiment that can discriminate between the two interactions will be significantly more sensitive than a similar detector that is not.

As mentioned throughout this chapter, even though the energy deposition processes of electronic and nuclear recoils are similar they are far from identical. These differences in track structure and interaction cross-sections lead to very large discrepancies in the amount of charge produced in an interaction relative to the amount of light produced at a given field. For energies relevant to the WIMP search, the relationship shown in Eqn. 2.18 holds for electronic and nuclear recoils and can be used to discriminate between them. Fig. 2.8 shows this difference between electronic and nuclear recoils for XENON1T with a drift field of $116.7 \pm 7.5\,{}^{\mathrm{V}}\!/\!_{\mathrm{cm}}$ [47].

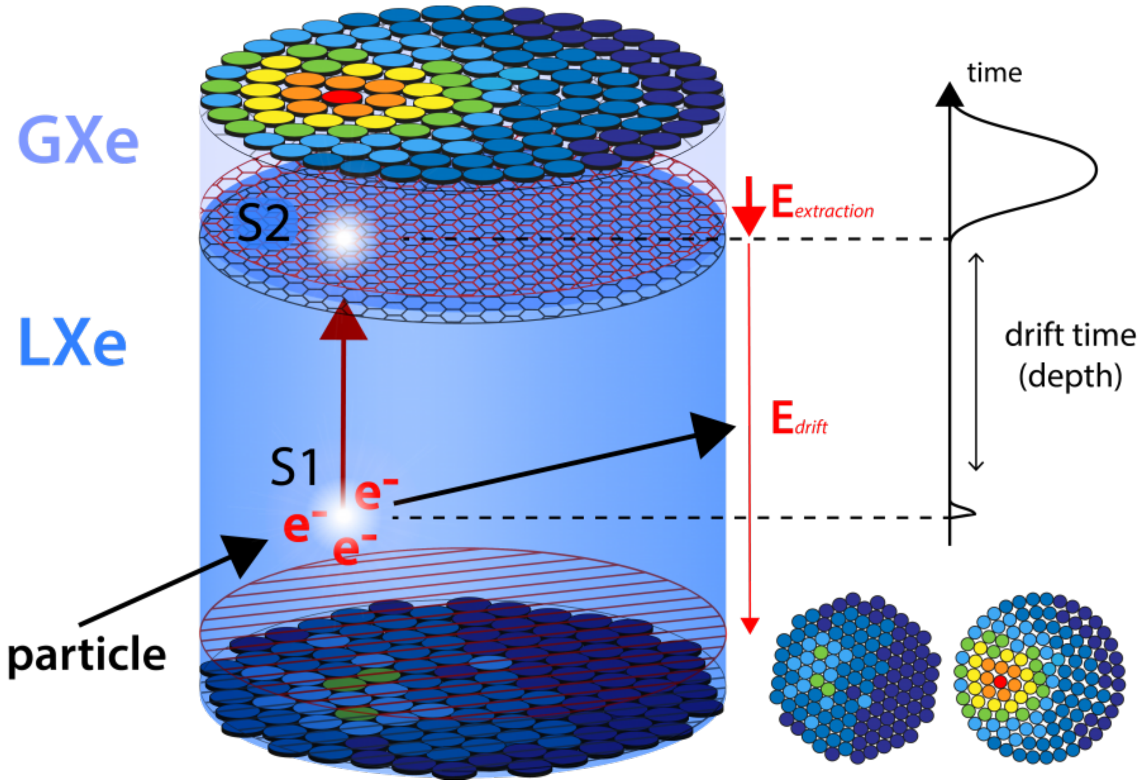

Figure 2.7: An example of an interaction in a dual-phase liquid xenon time projection chamber. The interaction produces both scintillation light and free electrons. The light is promptly detected by the PMT arrays at the top and bottom of the detector while the free electrons are drifted to the liquid-gas interface where they are extracted and accelerated through the gaseous xenon. This acceleration through the gaseous xenon causes secondary excitations that result in more scintillation light that is detected by the PMT arrays. The time difference between these interactions can be used to extract the depth of the interaction while the PMT hit patterns for the secondary signal can be used to find the interactions position in the transverse plane.

$$\left(\frac{\mathrm{S2}}{\mathrm{S1}}\right)_{\mathrm{ER}} > \left(\frac{\mathrm{S2}}{\mathrm{S1}}\right)_{\mathrm{NR}} \tag{2.18}$$

This difference in the ratio of charge to light can actually be enhanced further: while $\frac{\mathrm{S2}}{\mathrm{S1}}$ for nuclear recoils has little to no dependence on the electric field applied in the TPC, $\frac{\mathrm{S2}}{\mathrm{S1}}$ for electronic recoils is heavily dependent on the electric field [61, 90], as can be seen in Fig. 2.9. Therefore, the discrimination power between the two types of interactions can be increased by increasing the electric field used in the TPC.

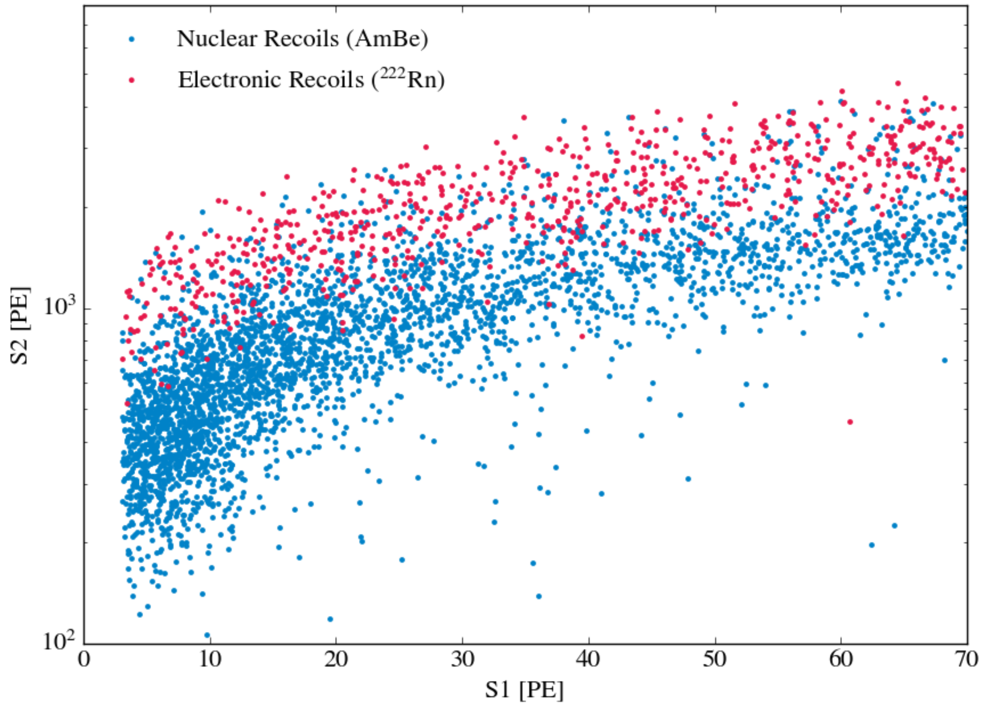

Figure 2.8: Low energy electronic and nuclear recoils in liquid xenon. Note that for a given S1 that the S2 for electronic recoils are usually significantly higher than the corresponding S2 for nuclear recoils. The nuclear recoils are from an americium-beryllium (AmBe) source while the electronic recoils are from the ^{222}Rn decay chain that results in a β^- emission with a maximum energy of 1.02 MeV.

Reconstructing Energy

A significant portion of this chapter was dedicated to understanding the production process of the observable photons and electrons in liquid xenon with an applied electric field. With a perfect understanding of the observables production process and the detector effects, one could reconstruct the probability distribution for the energy of an event. The reason you could not say the energy precisely, even with a perfect understanding of the physical processes described and the detector physics, is because there is an associated smearing at each stage in the observables process – in other words, two nuclear recoils depositing 10 keV at the same position in the detector will not produce exactly the same measured event each time.

However, even being able to approximate the energy of an event is extremely im-

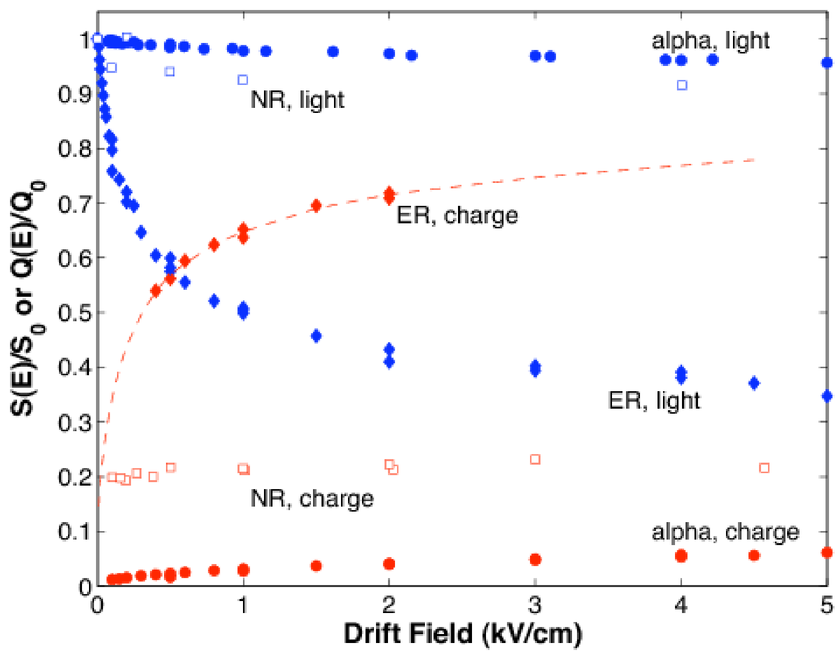

Figure 2.9: The field dependence of scintillation and ionization yield in liquid xenon for 122 keV electronic recoils and 56.5 keV nuclear recoils. In blue are the light yields of interactions at a given field relative to the light yield with no applied electric field. In red are the charge yields of interactions relative to the charge yield assuming no recombination. Image Credit: Ref. [61]

portant. More precisely, an understanding of the process between energy deposition to the readout of observables is essential for the most sensitive dark matter searches. The reason for this is because all predicted signals in the detector, including both background and potential WIMP signals, have a predictable energy spectrum. Therefore, we can not only predict how many electronic and nuclear recoils there should be but we can also say *where* they should be in an S1 and S2 spectrum. As a concrete example, we expect the nuclear recoil background to fall off exponentially with increasing energy. Therefore, an excess of events at high energies is more significant (or indicates a misunderstanding regarding the background) than an excess of events at low energies.

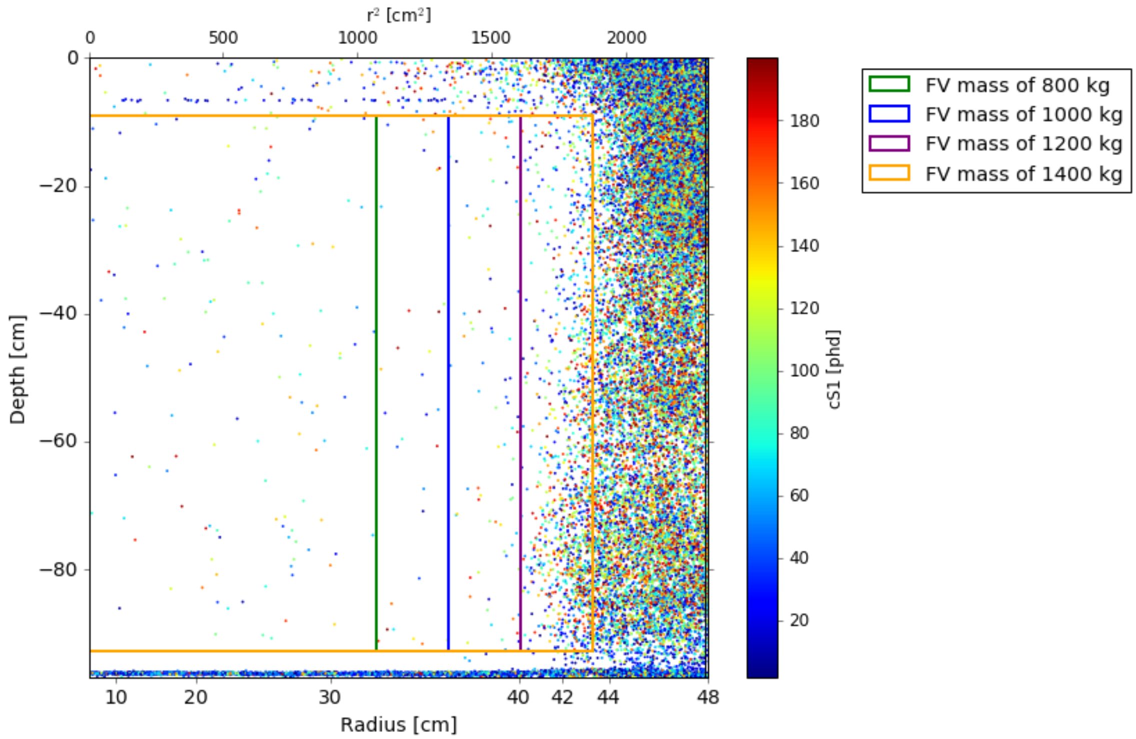

Figure 2.10: The positions of all events during the first science run of XENON1T. Notice that the overwhelming majority of events occur at the very edge of the detector and can be removed using a fiducial volume.

Reconstructing Position

An additional piece of information that proves to be very useful that can be extracted from TPCs is the the position of an event. As mentioned earlier, an approximately uniform electric field is applied in the TPC to extract the electrons created in an interaction from the vertex to the liquid-gas interface where they will produce the secondary signal, the S2. Of course, the scintillation light from the interaction is measured extremely quickly (on the order of nanoseconds such that we approximate the delay as zero) so the S1 can be used as the start of a timer that ends with the S2. This drift time can then be used to reconstruct the depth of the interaction since the electron will travel with a constant velocity through the liquid xenon as given by $v_d = \mu E$, where v_d is the drift velocity, μ is the mobility of electrons in liquid xenon, and E is the electric field applied. This analysis to determine the depth is shown on the right side of Fig. 2.7.

As mentioned earlier in this chapter, the stopping power for different charged particles in liquid xenon is high enough such that interactions will be stopped in $\lesssim 10\,\mu$m. Diffusion for electrons in liquid xenon is also small: even assuming a very large drift time of 1 ms, the expected transverse diffusion is on the order of $\sqrt{D_t t_d} \sim$ 20 mm so the electrons should still be very localized when arriving at the liquid-gas interface. Once these electrons are accelerated through the gas layer they create the secondary photons (S2), which are then detected using the PMT arrays at the top and the bottom of the detector. The hit pattern of the PMT arrays, specifically the top array, can be used to approximate the location of extraction at the liquid-gas interface, which should be a very good approximation of the position at the depth found using the drift time. The PMT hit patterns are shown on the bottom-right of Fig. 2.7.

The three-dimensional location of an event inside a detector proves to be very important for WIMP searches. To understand why, it is useful to consider a WIMP event in a detector. Since the cross-section of the WIMP is so small, one would expect two features in a WIMP event: it would only scatter a single time and that it could scatter anywhere in the liquid xenon with equal probability. However, this is very different from almost all of our external background sources (the exception, of course, being neutrinos) - both external gamma, beta, and neutron sources that emit particles into the liquid xenon are expected to lose energy through multiple scatters, which can easily be identified and removed by observing multiple S2 peaks (called a *multiple scatter cut*), and/or are expected to travel only a short distance before depositing all of their energy. The latter effect can be seen in Fig. 2.10, taken from XENON1T's first science run, which shows that the overwhelming majority of events occur at the very edges of the TPC. One can then remove these events by making a *fiducial volume cut* that removes all events not within a certain distance from the center of the detector — four of these potential fiducial volume cuts are shown in Fig. 2.10. By using a multiple scatter cut and a fiducial volume cut, it is straightforward to remove almost all of the external background events, although it is important to note that this will not remove events from internal sources such as

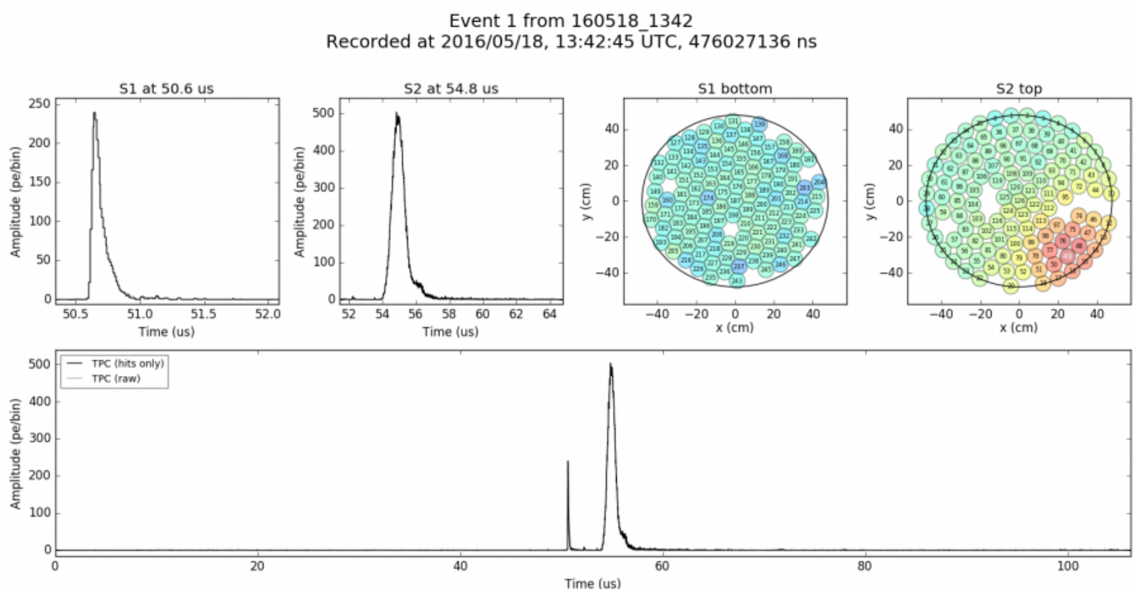

Figure 2.11: The waveform of the first event seen by XENON1T.

^{85}Kr or ^{222}Rn or events from neutrino interactions.

2.5.2 Detecting Observables

In this section we will discuss the details of how the observables produced by an interaction, the light and charge, are actually measured in TPCs to produce *waveforms* like the one shown in Fig. 2.11.

Detection of Scintillation Photons: S1

The excited xenon dimers, excimers, decay very quickly (on the order of 10 ns) and produce 178 nm photons regardless of the interaction type. These photons can be detected by the use of photomultiplier tubes (PMTs) that are designed to have peak efficiency for UV light. In TPCs, the PMT arrays are placed at the top and bottom of the detector, as shown in Fig. 2.7, but cannot be placed around the sides of the TPC as the high voltage of the PMTs will prevent the electric field used to drift the electrons from being uniform in the vertical direction. Because of this, light will typically reflect off of multiple surfaces before reaching the face of the PMT. Since detectable light is lost during reflections, the position of the event will be important in understanding

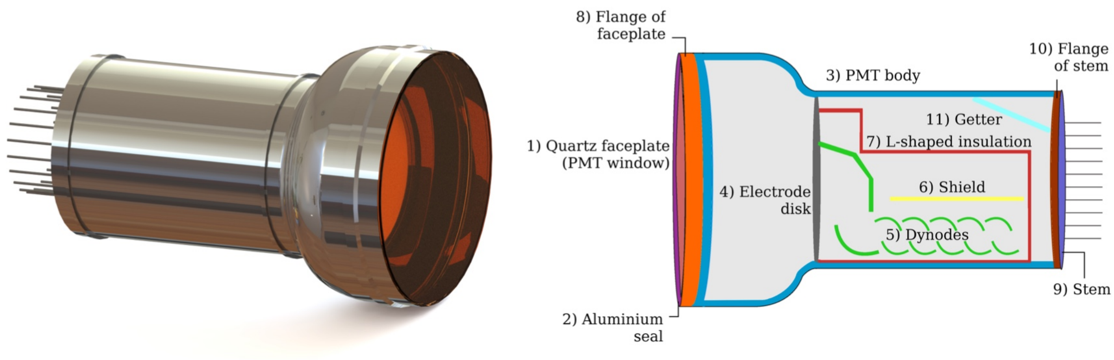

Figure 2.12: The Hamamatsu R11410 PMT and a schematic illustration of its various components. Image Credit: Ref. [94].

how much of the initial light is likely to be detected (with events closer to the PMTs and towards the center having a high detection efficiency than events near the edge of the TPC). There is also an efficiency loss in the PMTs themselves since only roughly a third of photons that reach the photocathode of the PMT produce a signal — this efficiency is referred to as the *quantum efficiency* (QE). These losses lead to roughly 90% of light from an interaction not being detected![5]

The main function of a PMT is to convert light signals into electrical signals, which can subsequently be digitized. A schematic of a photomultiplier tube is shown in Fig. 2.12. When light shines upon the PMT window, there is a probability defined by the quantum efficiency that an electron is emitted by the photoelectric effect — this electron is called a photoelectron. This photoelectron is then guided and accelerated by an electric field to a stage of dynodes by which the initial electron produces secondary electrons at each stage in the chain. The electrons reaching the end of the stage will be proportional to the initial number of photoelectrons and result in a current that can be digitized.

Since both the dexcitation of the excimers and the photomultiplication are both very fast processes (on the order of 10 ns), the S1 signal is considered to be a prompt signal. This is very different from the S2 signal which will have a long delay (on the

[5]Because of this large loss of scintillation light, a great deal of effort has gone into choosing and preparing material for the TPC to maximize the reflectivity [91–93].

order of tens to hundreds of microseconds) depending on the depth of the interaction in the liquid xenon and the strength of the applied drift field.

Detection of Ionization Electrons: S2

The S2 signal is a result of the electrons that do not recombine with an ion that was also created in the interaction. These electrons are drifted using an approximately uniform vertical electric field to the liquid-gas interface and then, using a second electric field typically much stronger than the drift field (thousands of $^{\mathrm{V}}/_{\mathrm{cm}}$ compared to hundreds), are extracted from the liquid and accelerated through the gas, as shown in Fig. 2.7. The accelerated electrons will create xenon excimers while being accelerated through the gas which will result in our secondary light signal that can be detected by PMTs.

The constant electron drift through the medium is actually an average over a series of many accelerations and decelerations. The electrons are accelerated by the electric field and quickly lose energy in the liquid xenon through elastic scatters [95]. While this complicated series of interactions on a macro scale is quite simple, there is a complicating factor: electrons drifting through the liquid can be absorbed by electronegative impurities in the xenon, the most common of which is oxygen. This process can also be examined from a larger scale and we can actually describe it with a single parameter: the so-called *electron lifetime*. The probability that an electron is not absorbed while drifting in the xenon is described in Eqn. 2.19.

$$P(z) = \frac{1}{\tau_{e^-}} e^{-\frac{z}{v_d \tau_{e^-}}} \tag{2.19}$$

In Eqn. 2.19, z is the vertical distance between the electron and liquid-gas interface, v_d is the drift velocity, and τ_{e^-} is the electron lifetime. The xenon in a TPC must be constantly cleaned of these electronegative impurities to maintain a reasonable electron lifetime which proves to be technically challenging. However, measuring the electron lifetime is relatively straight-forward. The basic idea is that you look at an electronic recoil of known energy (the electronic recoil resulting from the decay of

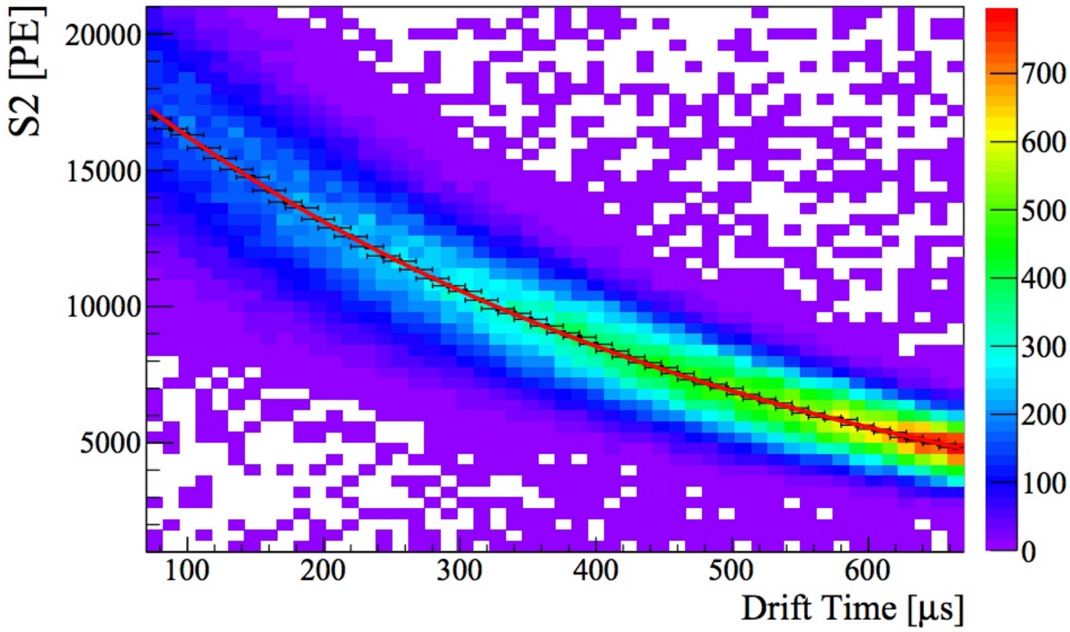

Figure 2.13: An example of an electron lifetime analysis from XENON1T. In this analysis, the 40 keV ^{83m}Kr electronic recoil is used and the decay's S2 signal size is plotted versus drift time (a proxy for depth). Image Credit: Ref. [96].

^{83m}Kr, for example) and look at the S2 signal as a function of depth. Since the light produced in the gaseous xenon is proportional to the number of electrons, one should see a decrease in the size of the S2 as a function of depth according to Eqn. 2.19. An example of this type of electron lifetime measurement is shown in Fig. 2.13. As detectors grow in size it is critical that they are still able to clean the xenon of the increased level of impurities still since a low electron lifetime results in a large reduction in signal and smearing in S2 (which reduces discrimination power).

Finally, the number of excitations produced in the gaseous xenon will be proportional to the number of electrons accelerated through. The resulting number of photons for a single electron approximately follows a Gaussian distribution. The mean of this Gaussian is referred to as the *gas gain*. Therefore, the number of electrons from the interaction can be inferred by looking at the number of photons detected by the photomultiplier tubes. This quantity can also be measured in a relatively simple manner by looking at single electrons that drift to the liquid-gas interface (these single electrons often come from the photoionization of the stainless steel grids used

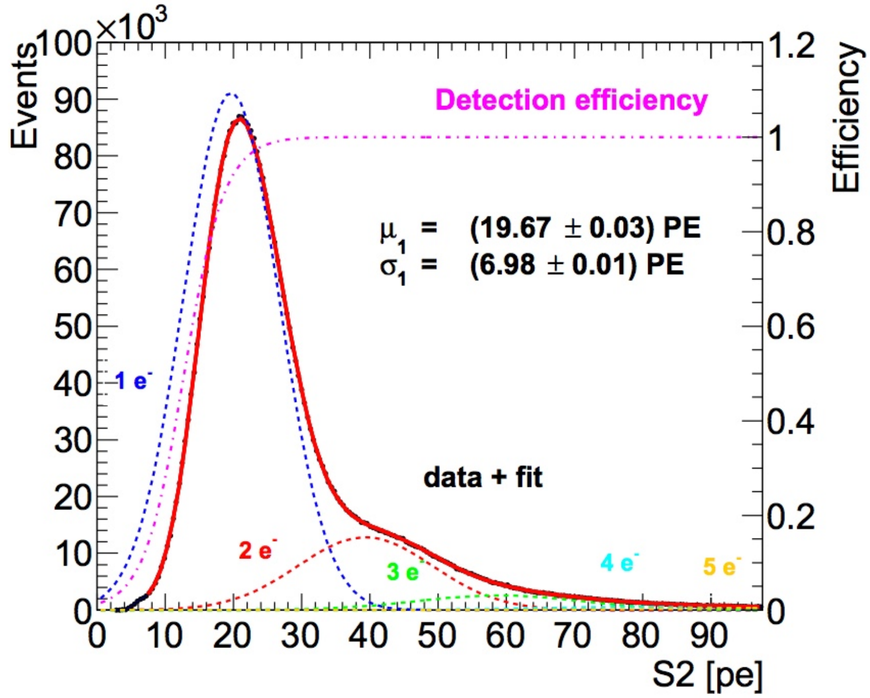

Figure 2.14: An example of a gas gain analysis from XENON100. This fit was performed using electrons from photoionization of metal inside of the detector. Image Credit: Ref. [97].

to produce the drift field in the TPC). This method is described in more detail in Ref. [97] and an example of this analysis is shown in Fig. 2.14.

Bibliography

[1] F. Zwicky, "The redshift of extragalactic nebulae," *Helv. Phys. Acta*, vol. 6, p. 110, 1933.

[2] K. Begeman, A. Broeils, and R. Sanders, "Extended rotation curves of spiral galaxies: dark haloes and modified dynamics," *Monthly Notices of the Royal Astronomical Society*, vol. 249, no. 3, pp. 523–537, 1991.

[3] V. C. Rubin and W. K. Ford Jr, "Rotation of the andromeda nebula from a spectroscopic survey of emission regions," *The Astrophysical Journal*, vol. 159, p. 379, 1970.

[4] D. Clowe, M. Bradač, A. H. Gonzalez, M. Markevitch, S. W. Randall, C. Jones, and D. Zaritsky, "A direct empirical proof of the existence of dark matter," *The Astrophysical Journal Letters*, vol. 648, no. 2, p. L109, 2006.

[5] A. A. Penzias and R. W. Wilson, "A measurement of excess antenna temperature at 4080 mc/s.," *The Astrophysical Journal*, vol. 142, pp. 419–421, 1965.

[6] D. Fixsen, E. Cheng, J. Gales, J. C. Mather, R. Shafer, and E. Wright, "The cosmic microwave background spectrum from the full cobe* firas data set," *The Astrophysical Journal*, vol. 473, no. 2, p. 576, 1996.

[7] P. A. Ade, V Salvatelli, V Stolyarov, F. Desert, J Knoche, M Giard, X Dupac, M Liguori, S Matarrese, Z Huang, *et al.*, "Planck 2015 results. xiii. cosmological parameters," *Astron. Astrophys.*, vol. 594, no. arXiv: 1502.01589, A13, 2015.

[8] C. L. Bennett, A. J. Banday, K. M. Górski, G Hinshaw, P Jackson, P Keegstra, A Kogut, G. F. Smoot, D. T. Wilkinson, and E. L. Wright, "Four-year cobe* dmr cosmic microwave background observations: maps and basic results," *The Astrophysical Journal Letters*, vol. 464, no. 1, p. L1, 1996.

[9] E. Komatsu, K. Smith, J Dunkley, C. Bennett, B Gold, G Hinshaw, N Jarosik, D Larson, M. Nolta, L Page, *et al.*, "Seven-year wilkinson microwave anisotropy probe (wmap*) observations: cosmological interpretation," *The Astrophysical Journal Supplement Series*, vol. 192, no. 2, p. 18, 2011.

[10] J. F. Navarro, “The structure of cold dark matter halos,” in *Symposium-international astronomical union*, Cambridge University Press, vol. 171, 1996, pp. 255–258.

[11] V. Springel, C. S. Frenk, and S. D. White, “The large-scale structure of the universe,” *arXiv preprint astro-ph/0604561*, 2006.

[12] M. Vogelsberger, S. Genel, V. Springel, P. Torrey, D. Sijacki, D. Xu, G. Snyder, D. Nelson, and L. Hernquist, “Introducing the illustris project: simulating the coevolution of dark and visible matter in the universe,” *Monthly Notices of the Royal Astronomical Society*, pp. 1518–1547, 2014.

[13] R. D. Peccei and H. R. Quinn, “Cp conservation in the presence of pseudoparticles,” *Physical Review Letters*, vol. 38, no. 25, p. 1440, 1977.

[14] A Alavi-Harati, I. Albuquerque, T Alexopoulos, M Arenton, K Arisaka, S Averitte, A. Barker, L. Bellantoni, A Bellavance, J Belz, *et al.*, “Observation of direct CP violation in $K_{S,L} \rightarrow \pi\pi$ decays,” *Physical Review Letters*, vol. 83, no. 1, p. 22, 1999.

[15] V Fanti, A Lai, D Marras, L Musa, A. Bevan, T. Gershon, B Hay, R. Moore, K. Moore, D. Munday, *et al.*, “A new measurement of direct CP violation in two pion decays of the neutral kaon,” *Physics Letters B*, vol. 465, no. 1, pp. 335–348, 1999.

[16] B. Aubert, D Boutigny, I De Bonis, J.-M. Gaillard, A Jeremie, Y Karyotakis, J. Lees, P Robbe, V Tisserand, A Palano, *et al.*, “Measurement of CP-violating asymmetries in B^0 decays to CP eigenstates,” *Physical Review Letters*, vol. 86, no. 12, p. 2515, 2001.

[17] K. Abe, R Abe, I Adachi, B. S. Ahn, H Aihara, M Akatsu, G Alimonti, K Asai, M Asai, Y Asano, *et al.*, “Observation of large CP violation in the neutral B meson system,” *Physical Review Letters*, vol. 87, no. 9, p. 091 802, 2001.

[18] R Aaij, C. A. Beteta, B Adeva, M Adinolfi, C Adrover, A Affolder, Z Ajaltouni, J Albrecht, F Alessio, M Alexander, *et al.*, “First observation of CP violation in the decays of B_s^0 mesons,” *Physical review letters*, vol. 110, no. 22, p. 221 601, 2013.

[19] P. W. Graham, I. G. Irastorza, S. K. Lamoreaux, A. Lindner, and K. A. van Bibber, “Experimental searches for the axion and axion-like particles,” *Annual Review of Nuclear and Particle Science*, vol. 65, pp. 485–514, 2015.

[20] I. Stern, “Admx status,” *arXiv preprint arXiv:1612.08296*, 2016.

[21] A. Garcon, D. Aybas, J. W. Blanchard, G. Centers, N. L. Figueroa, P. Graham, D. F. J. Kimball, S. Rajendran, M. G. Sendra, A. O. Sushkov, *et al.*, "Searching for dark matter with nuclear magnetic resonance: the cosmic axion spin precession experiment," *arXiv preprint arXiv:1707.05312*, 2017.

[22] G. Jungman, M. Kamionkowski, and K. Griest, "Supersymmetric dark matter," *Physics Reports*, vol. 267, no. 5-6, pp. 195–373, 1996.

[23] G. Bertone, *Particle dark matter: Observations, models and searches.* Cambridge University Press, 2010.

[24] X.-J. Bi, P.-F. Yin, and Q. Yuan, "Status of dark matter detection," *Frontiers of Physics*, vol. 8, no. 6, pp. 794–827, 2013.

[25] J. Stadel, D. Potter, B. Moore, J. Diemand, P. Madau, M. Zemp, M. Kuhlen, and V. Quilis, "Quantifying the heart of darkness with ghalo–a multibillion particle simulation of a galactic halo," *Monthly Notices of the Royal Astronomical Society: Letters*, vol. 398, no. 1, pp. L21–L25, 2009.

[26] A. V. Macciò, A. A. Dutton, F. C. Van Den Bosch, B. Moore, D. Potter, and J. Stadel, "Concentration, spin and shape of dark matter haloes: scatter and the dependence on mass and environment," *Monthly Notices of the Royal Astronomical Society*, vol. 378, no. 1, pp. 55–71, 2007.

[27] J. Read, "The local dark matter density," *Journal of Physics G: Nuclear and Particle Physics*, vol. 41, no. 6, p. 063 101, 2014.

[28] B. Zitzer *et al.*, "Search for dark matter from dwarf galaxies using veritas," *arXiv preprint arXiv:1509.01105*, 2015.

[29] J. Conrad, "Indirect detection of wimp dark matter: a compact review," *arXiv preprint arXiv:1411.1925*, 2014.

[30] F. S. Queiroz, "Dark matter overview: collider, direct and indirect detection searches," *arXiv preprint arXiv:1605.08788*, 2016.

[31] J. Kopp, V. Niro, T. Schwetz, and J. Zupan, "Dama/libra data and leptonically interacting dark matter," *Physical Review D*, vol. 80, no. 8, p. 083 502, 2009.

[32] J. Lewin and P. Smith, "Review of mathematics, numerical factors, and corrections for dark matter experiments based on elastic nuclear recoil," *Astroparticle Physics*, vol. 6, no. 1, pp. 87–112, 1996.

[33] T. M. Undagoitia and L. Rauch, “Dark matter direct-detection experiments,” *Journal of Physics G: Nuclear and Particle Physics*, vol. 43, no. 1, p. 013 001, 2015.

[34] T. Piffl, C. Scannapieco, J. Binney, M. Steinmetz, R.-D. Scholz, M. E. Williams, R. S. De Jong, G. Kordopatis, G. Matijevič, O. Bienayme, *et al.*, “The rave survey: the galactic escape speed and the mass of the milky way,” *Astronomy & Astrophysics*, vol. 562, A91, 2014.

[35] M. Kuhlen, N. Weiner, J. Diemand, P. Madau, B. Moore, D. Potter, J. Stadel, and M. Zemp, “Dark matter direct detection with non-maxwellian velocity structure,” *Journal of Cosmology and Astroparticle Physics*, vol. 2010, no. 02, p. 030, 2010.

[36] J Engel, “Nuclear form factors for the scattering of weakly interacting massive particles,” *Physics Letters B*, vol. 264, no. 1-2, pp. 114–119, 1991.

[37] R Strauss, G Angloher, A Bento, C Bucci, L Canonica, X Defay, A Erb, F. v. Feilitzsch, N. F. Iachellini, P Gorla, *et al.*, “Exploring low-mass dark matter with cresst,” *Journal of Low Temperature Physics*, vol. 184, no. 3-4, pp. 866–872, 2016.

[38] C Amole, M Ardid, I. J. Arnquist, D. M. Asner, D Baxter, E Behnke, P Bhattacharjee, H Borsodi, M Bou-Cabo, P Campion, *et al.*, “Dark matter search results from the pico- 60 c 3 f 8 bubble chamber,” *Physical review letters*, vol. 118, no. 25, p. 251 301, 2017.

[39] R Bernabei, P Belli, F Cappella, R Cerulli, C. Dai, A d’Angelo, H. He, A Incicchitti, X. Ma, F Montecchia, *et al.*, “Particle dark matter and dama/libra,” in *AIP Conference Proceedings*, AIP, vol. 1223, 2010, pp. 50–59.

[40] C. Aalseth, P. Barbeau, J. D. Leon, J. Fast, T. Hossbach, A Knecht, M. Kos, M. Marino, H. Miley, M. Miller, *et al.*, “Maximum likelihood signal extraction method applied to 3.4 years of cogent data,” *arXiv preprint arXiv:1401.6234*, 2014.

[41] X. collaboration *et al.*, “Direct dark matter search by annual modulation in xmass-i,” *Physics Letters B*, vol. 759, pp. 272–276, 2016.

[42] E Aprile, J Aalbers, F Agostini, M Alfonsi, F. Amaro, M Anthony, F Arneodo, P Barrow, L Baudis, B. Bauermeister, *et al.*, “Search for electronic recoil event rate modulation with 4 years of xenon100 data,” *Physical Review Letters*, vol. 118, no. 10, p. 101 101, 2017.

[43] T Heindl, T Dandl, A Fedenev, M Hofmann, R Krücken, L Oberauer, W Potzel, J Wieser, and A Ulrich, “Table-top setup for investigating the scintillation properties of liquid argon,” *Journal of Instrumentation*, vol. 6, no. 02, P02011, 2011.

[44] P.-A. Amaudruz, M Baldwin, M Batygov, B Beltran, C. Bina, D Bishop, J Bonatt, G Boorman, M. Boulay, B Broerman, *et al.*, “First results from the deap-3600 dark matter search with argon at snolab,” *arXiv preprint arXiv:1707.08042*, 2017.

[45] C. Aalseth, P. Barbeau, J Colaresi, J. Collar, J. D. Leon, J. Fast, N. Fields, T. Hossbach, A Knecht, M. Kos, *et al.*, “Search for an annual modulation in three years of cogent dark matter detector data,” *arXiv preprint arXiv:1401.3295*, 2014.

[46] E Armengaud, Q Arnaud, C Augier, A Benoit, L Bergé, T Bergmann, J Billard, J Blümer, T De Boissière, G Bres, *et al.*, “Constraints on low-mass wimps from the edelweiss-iii dark matter search,” *Journal of Cosmology and Astroparticle Physics*, vol. 2016, no. 05, p. 019, 2016.

[47] E Aprile, J Aalbers, F Agostini, M Alfonsi, F. Amaro, M Anthony, F Arneodo, P Barrow, L Baudis, B Bauermeister, *et al.*, “First dark matter search results from the xenon1t experiment,” *arXiv preprint arXiv:1705.06655*, 2017.

[48] P.-I. Collaboration, X. Cui, A. Abdukerim, W. Chen, X. Chen, Y. Chen, B. Dong, D. Fang, C. Fu, K. Giboni, *et al.*, “Dark matter results from 54-ton-day exposure of pandax-ii experiment,” *arXiv preprint arXiv:1708.06917*, 2017.

[49] R Agnese, A. Anderson, M Asai, D Balakishiyeva, D Barker, R. B. Thakur, D. Bauer, J Billard, A Borgland, M. Bowles, *et al.*, “Improved wimp-search reach of the cdms ii germanium data,” *Physical Review D*, vol. 92, no. 7, p. 072 003, 2015.

[50] C. Savage, G. Gelmini, P. Gondolo, and K. Freese, “Compatibility of dama/libra dark matter detection with other searches,” *Journal of Cosmology and Astroparticle Physics*, vol. 2009, no. 04, p. 010, 2009.

[51] A. Tan, M. Xiao, X. Cui, X. Chen, Y. Chen, D. Fang, C. Fu, K. Giboni, F. Giuliani, H. Gong, *et al.*, “Dark matter results from first 98.7 days of data from the pandax-ii experiment,” *Physical review letters*, vol. 117, no. 12, p. 121 303, 2016.

[52] D. Akerib, S Alsum, H. Araújo, X Bai, A. Bailey, J Balajthy, P Beltrame, E. Bernard, A Bernstein, T. Biesiadzinski, *et al.*, “Results from a search for dark

matter in the complete lux exposure," *Physical Review Letters*, vol. 118, no. 2, p. 021 303, 2017.

[53] G Angloher, A Bento, C Bucci, L Canonica, X Defay, A Erb, F von Feilitzsch, N. F. Iachellini, P Gorla, A Gütlein, *et al.*, "Results on light dark matter particles with a low-threshold cresst-ii detector," *The European Physical Journal C*, vol. 76, no. 1, p. 25, 2016.

[54] F Ruppin, J Billard, E Figueroa-Feliciano, and L Strigari, "Complementarity of dark matter detectors in light of the neutrino background," *Physical Review D*, vol. 90, no. 8, p. 083 510, 2014.

[55] J. Albert, M Auger, D. Auty, P. Barbeau, E Beauchamp, D Beck, V Belov, C Benitez-Medina, J Bonatt, M Breidenbach, *et al.*, "Improved measurement of the 2 $\nu\beta\beta$ half-life of 136 xe with the exo-200 detector," *Physical Review C*, vol. 89, no. 1, p. 015 502, 2014.

[56] K Ni, R Hasty, T. Wongjirad, L Kastens, A Manzur, and D. McKinsey, "Preparation of neutron-activated xenon for liquid xenon detector calibration," *Nuclear Instruments and Methods in Physics Research Section A: Accelerators, Spectrometers, Detectors and Associated Equipment*, vol. 582, no. 2, pp. 569–574, 2007.

[57] K Abe, J Hosaka, T Iida, M Ikeda, K Kobayashi, Y Koshio, A Minamino, M Miura, S Moriyama, M Nakahata, *et al.*, "Distillation of liquid xenon to remove krypton," *Astroparticle Physics*, vol. 31, no. 4, pp. 290–296, 2009.

[58] E Aprile, J Aalbers, F Agostini, M Alfonsi, F. Amaro, M Anthony, F Arneodo, P Barrow, L Baudis, B. Bauermeister, *et al.*, "Removing krypton from xenon by cryogenic distillation to the ppq level," *The European Physical Journal C*, vol. 77, no. 5, p. 275, 2017.

[59] N Barros, J Thurn, and K Zuber, "Double beta decay searches of 134xe, 126xe and 124xe with large scale xe detectors," *Journal of Physics G: Nuclear and Particle Physics*, vol. 41, no. 11, p. 115 105, 2014.

[60] D. W. Rankin, *Crc handbook of chemistry and physics, edited by david r. lide*, 2009.

[61] E. Aprile, C. Dahl, L de Viveiros, R. Gaitskell, K.-L. Giboni, J Kwong, P Majewski, K Ni, T Shutt, and M Yamashita, "Simultaneous measurement of ionization and scintillation from nuclear recoils in liquid xenon for a dark matter experiment," *Physical review letters*, vol. 97, no. 8, p. 081 302, 2006.

[62] A. Hitachi, T. Takahashi, N. Funayama, K. Masuda, J. Kikuchi, and T. Doke, "Effect of ionization density on the time dependence of luminescence from liquid argon and xenon," *Physical Review B*, vol. 27, no. 9, p. 5279, 1983.

[63] T. Doke, A. Hitachi, J. Kikuchi, K. Masuda, H. Okada, and E. Shibamura, "Absolute scintillation yields in liquid argon and xenon for various particles," *Japanese journal of applied physics*, vol. 41, no. 3R, p. 1538, 2002.

[64] J. Lindhard, V Nielsen, M Scharff, and P. Thomsen, "Integral equations governing radiation effects," *Mat. Fys. Medd. Dan. Vid. Selsk*, vol. 33, no. 10, pp. 1–42, 1963.

[65] A. Hitachi, "Properties of liquid xenon scintillation for dark matter searches," *Astroparticle Physics*, vol. 24, no. 3, pp. 247–256, 2005.

[66] W. Cottingham and D. Greenwood, *An Introduction to Nuclear Physics*. Cambridge University Press, 1987.

[67] J Mantel, "The beta ray spectrum and the average beta energy of several isotopes of interest in medicine and biology," *The International journal of applied radiation and isotopes*, vol. 23, no. 9, pp. 407–413, 1972.

[68] E Aprile, J Aalbers, F Agostini, M Alfonsi, F. Amaro, M Anthony, F Arneodo, P Barrow, L Baudis, B. Bauermeister, *et al.*, "Results from a calibration of xenon100 using a source of dissolved radon-220," *Physical Review D*, vol. 95, no. 7, p. 072 008, 2017.

[69] D. Akerib, H. Araújo, X Bai, A. Bailey, J Balajthy, P Beltrame, E. Bernard, A Bernstein, T. Biesiadzinski, E. Boulton, *et al.*, "Tritium calibration of the lux dark matter experiment," *Physical Review D*, vol. 93, no. 7, p. 072 009, 2016.

[70] E Aprile, J Aalbers, F Agostini, M Alfonsi, F. Amaro, M Anthony, F Arneodo, P Barrow, L Baudis, B Bauermeister, *et al.*, "Signal yields of kev electronic recoils and their discrimination from nuclear recoils in liquid xenon," *arXiv preprint arXiv:1709.10149*, 2017.

[71] G. F. Knoll, *Radiation detection and measurement*. John Wiley & Sons, 2010.

[72] M. Berger, "Xcom: photon cross sections database," *NIST Standard Reference Database 8 (XGAM)*,

[73] M. Chadwick, M Herman, P Obložinskỳ, M. E. Dunn, Y Danon, A. Kahler, D. L. Smith, B Pritychenko, G. Arbanas, R Arcilla, *et al.*, "Endf/b-vii. 1 nuclear data for science and technology: cross sections, covariances, fission product yields and decay data," *Nuclear Data Sheets*, vol. 112, no. 12, pp. 2887–2996, 2011.

[74] J. Timar, Z. Elekes, and B. Singh, “Nuclear data sheets for a= 129,” *Nuclear Data Sheets*, vol. 121, pp. 143–394, 2014.

[75] Y. Khazov, I Mitropolsky, and A Rodionov, “Nuclear data sheets for a= 131,” *Nuclear Data Sheets*, vol. 107, no. 11, pp. 2715–2930, 2006.

[76] E Aprile, J Aalbers, F Agostini, M Alfonsi, F. Amaro, M Anthony, L Arazi, F Arneodo, C Balan, P Barrow, *et al.*, “Physics reach of the xenon1t dark matter experiment.,” *Journal of Cosmology and Astroparticle Physics*, vol. 2016, no. 04, p. 027, 2016.

[77] T. Franarin and M. Fairbairn, “Reducing the solar neutrino background in dark matter searches using polarized helium-3,” *Physical Review D*, vol. 94, no. 5, p. 053 004, 2016.

[78] E. Dahl, “The physics of background discrimination in liquid xenon, and first results from xenon10 in the hunt for wimp dark matter.,” PhD thesis, Princeton University, 2009.

[79] T. Takahashi, S Konno, T Hamada, M. Miyajima, S. Kubota, A Nakamoto, A. Hitachi, E. Shibamura, and T. Doke, “Average energy expended per ion pair in liquid xenon,” *Physical Review A*, vol. 12, no. 5, p. 1771, 1975.

[80] E Aprile, K. Giboni, P Majewski, K Ni, and M Yamashita, “Observation of anticorrelation between scintillation and ionization for mev gamma rays in liquid xenon,” *Physical Review B*, vol. 76, no. 1, p. 014 115, 2007.

[81] J. B. Birks, *The Theory and Practice of Scintillation Counting: International Series of Monographs in Electronics and Instrumentation*. Elsevier, 2013, vol. 27.

[82] J Thomas and D. Imel, “Recombination of electron-ion pairs in liquid argon and liquid xenon,” *Physical Review A*, vol. 36, no. 2, p. 614, 1987.

[83] J Angle, E Aprile, F Arneodo, L Baudis, A Bernstein, A. Bolozdynya, L. Coelho, C. Dahl, L DeViveiros, A. Ferella, *et al.*, “Search for light dark matter in xenon10 data,” *Physical Review Letters*, vol. 107, no. 5, p. 051 301, 2011.

[84] P. Sorensen and C. E. Dahl, “Nuclear recoil energy scale in liquid xenon with application to the direct detection of dark matter,” *Physical Review D*, vol. 83, no. 6, p. 063 501, 2011.

[85] B. Lenardo, K. Kazkaz, A. Manalaysay, J. Mock, M. Szydagis, and M. Tripathi, “A global analysis of light and charge yields in liquid xenon,” *IEEE Transactions on Nuclear Science*, vol. 62, no. 6, pp. 3387–3396, 2015.

[86] G Jaffé, "On the theory of ionization in columns," *Ann. Phys.(Leipzig)*, vol. 42, pp. 303–344, 1913.

[87] D.-M. Mei, Z.-B. Yin, L. Stonehill, and A. Hime, "A model of nuclear recoil scintillation efficiency in noble liquids," *Astroparticle Physics*, vol. 30, no. 1, pp. 12–17, 2008.

[88] V. Tretyak, "Semi-empirical calculation of quenching factors for ions in scintillators," *Astroparticle physics*, vol. 33, no. 1, pp. 40–53, 2010.

[89] F. Bezrukov, F. Kahlhoefer, and M. Lindner, "Interplay between scintillation and ionization in liquid xenon dark matter searches," *Astroparticle Physics*, vol. 35, no. 3, pp. 119–127, 2011.

[90] L. Goetzke, E Aprile, M Anthony, G Plante, and M Weber, "Measurement of light and charge yield of low-energy electronic recoils in liquid xenon," *arXiv preprint arXiv:1611.10322*, 2016.

[91] C Silva, J Pinto da Cunha, V Chepel, V Solovov, F Neves, A Pereira, and M. Lopes, "Reflectance of polytetrafluoroethylene (ptfe) for xenon scintillation light," *J. Appl. Phys.*, vol. 107, no. arXiv: 0910.1056, p. 064 902, 2009.

[92] J. Haefner, A. Neff, M. Arthurs, E. Batista, D. Morton, M. Okunawo, K. Pushkin, A. Sander, S. Stephenson, Y. Wang, *et al.*, "Reflectance dependence of polytetrafluoroethylene on thickness for xenon scintillation light," *Nuclear Instruments and Methods in Physics Research Section A: Accelerators, Spectrometers, Detectors and Associated Equipment*, vol. 856, pp. 86–91, 2017.

[93] F Neves, A Lindote, A Morozov, V Solovov, C Silva, P Bras, J. Rodrigues, and M. Lopes, "Measurement of the absolute reflectance of polytetrafluoroethylene (ptfe) immersed in liquid xenon," *Journal of Instrumentation*, vol. 12, no. 01, P01017, 2017.

[94] E Aprile, F Agostini, M Alfonsi, L Arazi, K Arisaka, F Arneodo, M Auger, C Balan, P Barrow, L Baudis, *et al.*, "Lowering the radioactivity of the photomultiplier tubes for the xenon1t dark matter experiment," *The European Physical Journal C*, vol. 75, no. 11, p. 546, 2015.

[95] V. Atrazhev, A. Berezhnov, D. Dunikov, I. Chernysheva, V. Dmitrenko, and G Kapralova, "Electron transport coefficients in liquid xenon," in *Dielectric Liquids, 2005. ICDL 2005. 2005 IEEE International Conference on*, IEEE, 2005, pp. 329–332.

[96] E. Aprile, J Aalbers, F Agostini, M Alfonsi, F. Amaro, M Anthony, B Antunes, F Arneodo, M Balata, P Barrow, *et al.*, "The xenon1t dark matter experiment," *arXiv preprint arXiv:1708.07051*, 2017.

[97] E Aprile, M Alfonsi, K Arisaka, F Arneodo, C Balan, L Baudis, B Bauermeister, A Behrens, P. Beltrame, K Bokeloh, *et al.*, "Observation and applications of single-electron charge signals in the xenon100 experiment," *Journal of Physics G: Nuclear and Particle Physics*, vol. 41, no. 3, p. 035 201, 2014.